Numerical diffusion and turbulent mixing in convective self-aggregation

L. Silvestri[1], M. Saraceni[1], P. Bongioannini Cerlini[2]

[1]University of Perugia, Department of Civil and Environmental Engineering (DICA) - Centro di Ricerca sul Clima e Cambiamenti Climatici (CRC), Perugia (PG)
[2]University of Perugia, Department of Physics and Geology - Centro di Ricerca sul Clima e Cambiamenti Climatici (CRC), Perugia (PG)

Key Points:

- A large horizontal variability of deep convection at large scales is necessary for drying the free troposphere and trigger convective self-aggregation;
- The strength of humidity perturbations introduced by convection in the free troposphere are regulated by the model small-scale implicit and explicit dissipation.
- Finer grid resolution allows the spontaneous development of convective self-aggregation when enough turbulent mixing is provided;

Corresponding author: Lorenzo Silvestri, `lorenzo.silvestri@unipg.it`

Abstract

Spontaneous aggregation of deep convection is a common feature of idealized numerical simulations of the tropical atmosphere in Radiative-Convective Equilibrium (RCE). However, at coarse grid resolution where deep convection is not fully resolved, the occurrence of this phenomenon is extremely sensitive to subgrid-scale processes. This study focuses on the role played by mixing and entrainment, either provided by the turbulence model or the implicit numerical dissipation. We have analyzed the results of two different models, WRF and SAM, and compared different configurations by varying the turbulence models, the initial conditions and the horizontal spatial resolution. At coarse grid resolution (3 km), the removal of turbulent mixing prevents the occurrence of Convective Self-Aggregation (CSA) in models with low numerical diffusivity, while it is preserved in models with high numerical diffusivity. When the horizontal grid resolution is refined to 1 km (thus reducing the implicit numerical dissipation), CSA is only achieved by increasing the explicit turbulent mixing. In this case, CSA was found to occur even with a small amount of shallow clouds. Therefore, this study suggests that the sensitivity of CSA to horizontal grid resolution is not primarily due to the corresponding decrease in shallow clouds. Instead, it is found that turbulent mixing and dissipation at small scales regulate the amplitude of initial humidity perturbations introduced by convection in the free troposphere: the greater the dissipation at small scales, the greater the size and the strength of humidity perturbations in the free troposphere that can destabilize the RCE state.

Plain Language Summary

Convection acts to transport moisture from the surface to the free troposphere and to form clouds. When clouds develop in a dry environment, they can be diluted by turbulent mixing. On the contrary, mixing in a moist environment favors their deepening. Therefore, turbulent mixing will favor convection over moist regions making them moister, while the opposite is true for dry regions. This is called the moisture-convection feedback (or moisture-entrainment-convection feedback). This feedback plays a relevant role in the creation of humidity perturbations in the free troposphere, by destabilizing the radiative-convective equilibrium state, where convection is homogeneously distributed, to a stable state where convection is clustered. This work analyzes this phenomenon, called Convective Self-Aggregation, and its sensitivity to turbulence models and implicit numerical dissipation, the main sources of mixing when using a grid resolution of O(1 km). In particular, it is found that large dissipation at small-scales, is necessary to develop large humidity fluctuations in the free-troposphere, which is a prerequisite for the creation of large dry areas free of convection. Therefore a correct representation of sub-grid scale mixing processes is necessary to capture the convective self-aggregation phenomenon in high-resolution climate models.

1 Introduction

In the absence of lateral energy transport, the atmosphere would be in a statistical Radiative Convective Equilibrium (RCE), where radiative cooling is balanced by convective heating. Despite large-scale dynamical forcings are ubiquitous in the real atmosphere, RCE can be observed in the tropics on a daily scale, when areas larger than 5000 km^2 are considered (Jakob et al., 2019).

Without heterogeneities in boundary conditions and forcing, idealized numerical simulations of RCE provide a simple framework to study the internal interactions between moist convection, radiation and circulation. In these simulations, the atmosphere is destabilized by a combination of surface heating and tropospheric radiative cooling. The Weak Temperature Gradient (WTG) hypothesis applies to the free troposphere and heating anomalies directly generates large-scale circulation that moisten (dry) the at-

mosphere by large-scale water vapor convergence (divergence). Deep convection develops uniformly throughout the domain, naturally reflecting the homogeneity of the external forcing. However, typically after few days, many numerical studies both with different Cloud-Resolving Models (CRMs) (Held et al., 1993; Tompkins, 2001; C. S. Bretherton et al., 2005; C. J. Muller & Held, 2012; Wing & Emanuel, 2014; Yanase et al., 2020) and various General Circulation Models (GCMs) (Wing et al., 2020) have shown a transition from the initial uniform state of convection to a state in which convection is clustered into a moist patch surrounded by a dry patch with suppressed convective activity. This process has been called convective self-aggregation (CSA), because it is caused by internal feedback between moisture, convection and radiation. When CSA occurs, the atmosphere dries out, large-scale circulation develop and outgoing longwave radiation (OLR) increases. All of this has important implications for climate. Moreover, in the presence of rotation, CSA becomes organized eddies and could be used as an idealized framework to study Tropical Cyclone Genesis (Nolan et al., 2007; Rappin et al., 2010; Wing et al., 2016; Ramírez Reyes & Yang, 2021; Carstens & Wing, 2022).

In idealized numerical simulations several physical processes have been found to be relevant for the onset of CSA which are distinct from the mechanisms responsible for its maintenance. In the following, only a brief overview of such processes is given, with emphasis on the onset of CSA. The reader is referred to C. Muller et al. (2022) and Wing et al. (2017) for a comprehensive review. Radiative and surface flux feedback contributes positively to clustering in the early stages of aggregation. Tompkins and Craig (1998) and C. S. Bretherton et al. (2005) were among the first to show that homogenizing radiative heating rates or assuming wind-insensitive surface fluxes prevents clustering. C. J. Muller and Held (2012) emphasized the importance of low-level longwave cooling in dry regions both from clear-sky and shallow clouds. The differential radiative cooling between moist and dry regions drives a low-level upgradient Moist Static Energy (MSE) circulation which expands dry regions and maintains self-aggregation. As a consequence, C. J. Muller and Held (2012) proposed the decrease of low-level cloudiness with finer horizontal resolutions as a possible explanation for the disappearance of CSA in simulations with horizontal grid sizes less than 1 km. The relevance of radiative feedback and the low-level MSE circulation was later quantified by Wing and Emanuel (2014) trough the analysis of the different budget terms (longwave and shortwave radiation, surface fluxes and advection) contributing to the increase of the column integral of Frozen Moist Static Energy (FMSE) variance. Based on these numerical results, Emanuel et al. (2014) developed a radiative-convective instability theory. This theory demonstrates how, within a WTG framework, an anomalous radiative cooling in the free troposphere (corresponding to a dry perturbation) generates subsidence motions that dry the atmosphere and further increase radiative cooling there, creating a feedback loop.

In addition to radiative and surface flux feedback, other studies have demonstrated the importance of boundary layer diabatic feedback. Jeevanjee and Romps (2013) found that inhibition of cold pools (by switching off rain evaporation) allow self aggregation to occur at all domain sizes. C. Muller and Bony (2015) found similar results even when radiative cooling rates were homogenized across the free troposphere. This "moisture-memory aggregation" can be reproduced by the simple coarsening model of Craig and Mack (2013) and has recently been found to occur spontaneously in models with a nearly saturated sub-cloud layer (Cerlini et al., 2023). Finally, D. Yang (2018) demonstrated that CSA could occur also with minimal ingredients by homogenizing radiative cooling over the entire column, switching off rain evaporation over the boundary layer and without interactive surface fluxes. More recently, Ramírez Reyes and Yang (2021) shows that also tropical cyclones can also be generated without radiative and surface flux feedback. Thus, in this minimal configuration, two remaining physical processes could explain the onset of CSA: the moisture convection (MC) feedback and the Convective Heating Overturning Circulation (CHOC) feedback.

The MC feedback, or more specifically the moisture-entrainment-convection feedback, involves high detrainment of moist air from deep convective cores locally moist-

ening the surrounding environment making it more prone to future convection than drier zones (Tompkins, 2001; Grabowski & Moncrieff, 2004). In numerical simulation with coarse horizontal resolution (order of 1 km) and explicit convection, mixing processes are largely controlled by the subgrid-scale (SGS) turbulence scheme. At such coarse grid resolution deep convection and turbulence motions inside clouds are not resolved and overturning circulations occur in a laminar mode (Bryan et al., 2003). Moreover at coarse grid resolutions, dissipation processes in cold pools (Grant & van den Heever, 2016) and shallow convection (Janssens et al., 2022), fundamental for the development of shallow circulations, may depend considerably on the choice of the model. Therefore the relevance of MC feedback in CSA could also be measured by its sensitivity to the SGS turbulence parametrization. While no sensitivity was found by C. J. Muller and Held (2012) with the SAM (the System for Atmospheric Modeling, M. F. Khairoutdinov & Randall, 2003) model, Tompkins and Semie (2017) found an opposite result with the WRF (the Weather Research and Forecasting Model, Skamarock et al., 2019) model. In particular, they found that a high mixing rate of water vapor (high eddy diffusivity) is a necessary condition for convective organization to occur. This result was also confirmed by the experiments of Shi and Fan (2021). Using Cloud Model 1 (CM1), they demonstrated that different turbulent parametrizations in the PBL can substantially affect the initiation of self-aggregation.

The CHOC feedback is that deep convection releases latent heat, that amplifies the existing positive buoyancy and pressure perturbations and the associated overturning circulation and therefore convection. This effect was diagnosed by D. Yang (2018) looking at the Available Potential Energy (APE) budget. D. Yang (2019) showed that the CHOC feedback was able to produce CSA even in the absence of the MC feedback. There, the MC feedback was eliminated by nudging clear-sky water vapor to its horizontal mean every 3 hours during the simulation. However, CSA without the MC feedback shows a much smaller increase in the variance of precipitable water and two different clusters rather than a single moist patch.

The above studies show contrasting results regarding the importance of Moisture-Convection Feedback for the onset of CSA. This paper supports the hypothesis of Tompkins and Semie (2017) that MC feedback and mixing processes are necessary for the onset of CSA and for the creation of large dry patches. It is demonstrated here that an efficient updraft dilution, either created by explicit or implicit mixing processes, encourages more large-scale variability of convection (Mapes & Neale, 2011) in the early stages and creates a large enough dry perturbation in the free troposphere to start the radiative feedback loops. Thus, small-scale mixing processes and their representation becomes fundamental to the establishment of free-tropospheric (FT) drying which is considered a prerequisite for the onset of CSA by creating a strong boundary layer cooling in dry regions (B. Yang & Tan, 2020; Shamekh et al., 2020; Yanase et al., 2022).

The fact that "large enough fluctuation in the humidity content has to be present for self-aggregation to start" was hypothesized by Windmiller and Craig (2019) and further confirmed by the idealized model of Biagioli and Tompkins (2023), but here it is shown to work with different CRMs. We also show how such perturbation varies with different horizontal grid sizes and how it can explain the sensitivity of CSA to horizontal resolution, independent of the amount of low-level cloud.

The paper is organized as follows. First, in Section 2, SAM and WRF numerical models are described by focusing particularly on the numerics (Section 2.1.1) and the subgrid-scale turbulence models (Section 2.1.2). In Section 2.2 the simulations setup is detailed and all main and sensitivity experiments are described. The results are divided into four sections. Section 3.1 focuses on the general characteristics of the self-aggregation state and its impact on domain-average statistics. Section 3.2 shows the analysis of power spectra for kinetic energy, humidity and temperature to quantify the horizontal variability of convection in the different simulations. Section 3.3 studies the relevance of MC feedback in the triggering of CSA, by introducing the effect of SGS mixing in the MSE budget analysis. Section 3.4 summarizes the hypothesized mechanism for triggering CSA and compares it with the radiative mechanisms as caused by the WTG hypothesis. The sen-

sitivity of the results to initial conditions, turbulent Pr number and horizontal resolution, is examined in Section 4. All results of the present study are discussed in Section 5 and concluding remarks are given in Section 6.

2 Material and methods

2.1 Numerical models

The two cloud-resolving models chosen for this work are the System of Atmospheric Modeling (SAM version 6.10.5; M. F. Khairoutdinov & Randall, 2003) and the Weather Research and Forecasting Model (WRF version 4.2.2; Skamarock et al., 2019). Such models offer a solid benchmark for studying the sensitivity of convective aggregation to turbulent and numerical diffusion because: 1) they are widely used across the scientific community; 2) they have different mathematical formulations, different numerics and different physics; 3) the mechanisms behind convective self-aggregation have already been investigated for both models (e.g., see Tompkins and Semie (2017); Colin et al. (2019); B. Yang and Tan (2020), for WRF and C. S. Bretherton et al. (2005); C. J. Muller and Held (2012); Wing and Emanuel (2014); D. Yang (2018); Patrizio and Randall (2019) for SAM); 4) both models participated to the RCEMIP project (Wing et al., 2020).

The SAM model solves the anelastic continuity, momentum, and scalar conservation equations. The prognostic thermodynamic variables are the total non precipitating water ($q_T = q_v + q_c + q_i$ = water vapor + cloud water + cloud ice), the total precipitating water ($q_p = q_r + q_s + q_g$ = rain + snow + graupel) and the liquid/ice static energy $h_L = c_p T + gz - L_v(q_c + q_r) - L_s(q_i + q_s + q_g)$, where L_v and L_s are the latent heat of vaporization and sublimation, respectively. Given h_L, q_T and q_p, the mixing ratio of the various hydrometeors (q_c, q_i, q_r, q_s, q_g) is diagnosed by partitioning relationships that depend only on temperature.

The WRF model has a different dynamical core since it solves the fully compressible conservation equations for mass, momentum, heat and water substance (water vapor, liquid, and ice). The thermodynamic prognostic variables are different from SAM since WRF conserves the moist potential temperature ($\theta_m \approx \theta(1+1.61q_v)$), the geopotential and the mixing ratio for the six water species (water vapor, q_v, cloud water, q_c, cloud ice, q_i, rain, q_r, snow, q_s and hail,q_h). As demonstrated by Kurowski et al. (2014), different model mathematical formulations (anelastic versus fully compressible models as considered in this study) have negligible impact on the simulation of moist deep convection. Therefore, we will assume that differences in model numerics and physical parametrizations will have a larger impact than those resulting from different mathematical frameworks. The differences in model numerics and subgrid-scale turbulence scheme are detailed on Section 2.1.1 and Section 2.1.2, respectively.

The other physical parametrization (microphysics, radiation, and surface layer) have been fixed to those used by C. J. Muller and Held (2012) for the SAM model and by (Tompkins & Semie, 2017, , see their smag3dpbl simulation in Table 1) for the WRF model, to make our results directly comparable to their work. All parametrizations used are summarized in Table 1.

2.1.1 Numerics

Both models use a staggered Arakawa C-type grid with stretched vertical and uniform horizontal grids. The main numerical schemes used for time integration, momentum, and scalar advection are described in Table 2. WRF integrates the compressible non-hydrostatic equation in conservative (flux) form by employing a split-explicit 3rd order RK scheme (Wicker & Skamarock, 2002). Such a scheme can be combined both with even-ordered (spatially centered) schemes or odd-ordered (upwind-biased) schemes to form a stable advection scheme. In our experiments, we use the WRF standard configuration by using an upwind-biased advection scheme with the 5th order in the horizontal and the 3rd order in the vertical, both for scalars and momentum. Then positive-

Table 1. Physics parametrizations adopted for the WRF and SAM model common to all numerical experiments as listed in Table 3.

Parametrization	SAM	WRF
Radiation	CAM3 (Collins et al., 2006)	RRTMG (Iacono et al., 2008)
Microphysics	SAM1MOM (M. F. Khairoutdinov & Randall, 2003)	Purdue Lin (Chen & Sun, 2002)
Surface layer	Monin-Obukhov similarity	Revised MM5 similarity (Jiménez & Dudhia, 2012)
Subgrid-scale turbulence	3D Smagorinsky	3D Smagorinsky (Smagorinsky, 1963)
PBL	None	Yonsei University, YSU (Hong et al., 2006)

definite and monotonic scalar flux renormalizations are applied on the final RK step as described in Skamarock and Weisman (2009); Wang et al. (2009). The adopted spatial discretization is equivalent to a centered scheme of the next higher order (e.g. 6th in the horizontal and 4th in the vertical) plus a diffusive term with a coefficient that is proportional to the advection speed. Therefore this implicit diffusion may be inadequate in light wind conditions as underlined by Knievel et al. (2007); Bryan (2005). Moreover, the atmosphere in RCE idealized simulations is conditionally unstable, therefore spurious perturbations introduced by the numerical scheme may grow further and affect deep convection.

To smooth out grid-scale noise, WRF has an optional 6th order explicit horizontal spatial filter which can be applied with or without the imposition of monotonicity (Knievel et al., 2007). In our main experiments, this filter is included without monotonicity, to be as coherent as possible to the simulations by Tompkins and Semie (2017) and to damp noise more selectively. However, without enforcing monotonicity, new oscillations could be introduced by the filter in the thermodynamic fields (Xue, 2000). The interaction between grid-scale numerical oscillations either introduced by oscillatory momentum numerics (as finite differences) or by the explicit filters could interact with the SGS turbulence model and lead to excessively large values of eddy diffusivity (Pressel et al., 2017).

Finally, all the experiments employ three other explicit filters which are included in the standard WRF configuration using the RK3 time integration scheme: the 3D divergence damping to damp acoustic waves and spurious noise associated with the time-split discretization; the external mode damping which is used to damp pressure oscillations which do not propagate in the vertical (also called external inertia-gravity wave); forward biasing of the vertically-implicit acoustic-time-step to damp instabilities associated with vertically-propagating sound waves. For a comprehensive review of all these types of filters and their application to General Circulation Models (GCMs) the reader is referred to Jablonowski and Williamson (2011).

The SAM anelastic equations are integrated in time with an explicit 3rd order Adam-Bashfort scheme (AB3). Momentum advection is performed by using a 2nd ordered centered differences (SOC) scheme in a flux form for kinetic energy conservation. In most studies of CSA (C. S. Bretherton et al., 2005; C. J. Muller & Held, 2012; Wing & Emanuel, 2014, e.g.), the scalar advection is based on the 2nd order accurate monotonic MPDATA scheme (Smolarkiewicz & Grabowski, 1990). However, in this work, we need as small numerical diffusion as possible. Therefore, we use the 5th order monotonic ULTIMATE-MACHO scheme as developed by Yamaguchi et al. (2011). In that study, running SAM in a simulation of deep convective clouds with such a higher-order scheme showed similar results as running the same simulation with a low-order advection scheme and in-

creased horizontal resolution (Yamaguchi et al., 2011). No explicit filters are employed in SAM.

Table 2. Numerical schemes adopted by the main experiments performed with the SAM and the WRF models.

	SAM	WRF
Time Integration	Explicit 3rd order Adam-Bashfort scheme	Split-explicit 3rd order RK scheme (Wicker & Skamarock, 2002)
Momentum Advection	2nd order centered finite differences	5th order upwind-biased horizontal; 3rd order upwind-biased vertical
Scalar Advection	5th order ULTIMATE-MACHO scheme (Yamaguchi et al., 2011)	5th order upwind-biased horizontal; 3rd order upwind-biased vertical
Explicit mixing	None	6th order numerical diffusion

2.1.2 Subgrid-scale turbulence

All the experiments which have a parametrization for SGS turbulence adopt the Smagorinsky-Lilly (Smagorinsky, 1963; Lilly, 1962) eddy-viscosity model. This turbulence closure was chosen mainly because it has been used by most of the convective self-aggregation studies involving the SAM model (C. S. Bretherton et al., 2005; C. J. Muller & Held, 2012; Wing & Emanuel, 2014) and the WRF model (Tompkins & Semie, 2017; Colin et al., 2019; B. Yang & Tan, 2020). Furthermore, this is a popular choice also for CSA studies performed with other models (to cite some Yanase et al. (2020), SCALE-RM; Holloway and Woolnough (2016), Met Office UM; Hohenegger and Stevens (2016), UCLA-LES).

Eddy viscosity models do not allow any energy transfer from the SGS scales to the resolved scales. They are purely dissipative and model the turbulent fluxes of momentum (the Reynolds stress term, $\tau_{ij} = \overline{u_i' u_j'}$, where u_i' is the velocity at subgrid scales) and other scalar quantities, ϕ, in the following form:

$$\tau_{ij} = -2K_{h,v}\overline{S}_{ij} \quad (1)$$

$$\tau_{\phi j} = -K_{h,v} Pr^{-1} \frac{\partial \overline{\phi}}{\partial x_j} \quad (2)$$

where the overbar denotes resolved quantities, $\overline{S}_{ij} = 1/2(\partial \overline{u}_i/\partial x_j + \partial \overline{u}_j/\partial x_i)$ is the resolved strain rate tensor and $K_{h,v}$ is the horizontal or vertical eddy viscosity, also called mixing coefficient and Pr is the turbulent Prandtl number. For both SAM and WRF we choose the anisotropic implementation of the Smagorinsky-Lilly closure, where two different mixing coefficients are specified for the horizontal and the vertical direction. The choice of an anisotropic rather than isotropic diffusion approach can have a large impact on the mesoscale organization. De Roode et al. (2022) simulated a clear convective boundary layer in the SAM model and compares the results of a well-resolved isotropic LES ($\Delta x = 12.5$ m) with that obtained by coarsening the grid up to 1.2 km either using isotropic or anisotropic diffusion approaches. In their study, the anisotropic diffusion approach was found to perform better than the isotropic for what concern the entrainment velocity at the top of the boundary layer (a parameter which has a strong impact on the onset of cloud formation, since more entrainment causes larger heating and drying rates of the boundary layer). However, while coarsening the horizontal grid, the simulations

with the anisotropic diffusion approach lead to a stronger dissipation of spectral energies at the largest wavenumbers that eventually leads to larger mesoscale fluctuations and an associated shift in the spectral energies toward smaller wavenumbers. Since the occurrence of CSA in coarse CRM (grid spacing exceeding 1 km) can be associated with an increase of kinetic energy and variance on small wavenumbers (Yanase et al., 2022; Janssens et al., 2022), grid anisotropy can be a relevant factor.

The definition of $K_{h,v}$ is slightly different between WRF and SAM. In WRF, using the notation by Simon and Chow (2021), it takes the following form:

$$K_h = (C_s l_h)^2 \overline{S}_\beta \tag{3}$$
$$K_v = (C_s l_v)^2 \overline{S}_\beta \tag{4}$$

with C_s being constant with a default value of 0.25. The horizontal and vertical mixing length scales, l_h and l_v respectively, are related to the grid spacing $(\Delta_x, \Delta_y, \Delta_z)$ as:

$$l_h = (\Delta_x \Delta_y)^{1/2} \tag{5}$$
$$l_v = \Delta_z \tag{6}$$

S_β in Eqs. 3 and 4 is the magnitude of the resolved strain rate tensor modified by a factor based on the local Richardson number, to reduce mixing coefficient on very stable atmospheric condition:

$$S_\beta = max\left[0, \left(\overline{S_{ij}}^2 - \frac{N^2}{Pr}\right)\right]^{1/2} \tag{7}$$

where N is the local moist Brunt-Väisäla frequency (following D. R. Durran and Klemp (1982)) and Pr is the turbulent Prandtl number, which is constant and equal to 1/3 in WRF. Upper and lower limits to the mixing coefficient are imposed horizontally as:

$$K_h^{min} = a_{min}(\Delta_x \Delta_y) \tag{8}$$
$$K_h^{max} = a_{max}(\Delta_x \Delta_y \Delta_t^{-1}) \tag{9}$$

and in the vertical as:

$$K_v^{min} = a_{min}(\Delta_z^2) \tag{10}$$
$$K_v^{max} = a_{max}(\Delta_z^2 \Delta_t^{-1}) \tag{11}$$

where $a_{min} = 10^{-6} s^{-1}$ and $a_{max} = 0.1$ are two constant factors and Δ_t is the time step.

Most of the time, when the horizontal grid spacing exceeds 100 m and boundary layer eddies are not well-resolved, the Smagorinsky-Lilly closure in WRF is used in conjunction with a Planetary Boundary Layer scheme (PBL). In such cases, the local standard vertical diffusion is deactivated and will be substituted by a non-local mixing coefficient over the whole mixed layer (whose height is diagnosed by the scheme itself). In our WRF configuration, we employ the YSU PBL (Hong et al., 2006), as done in other studies of CSA Tompkins and Semie (2017); B. Yang and Tan (2020); Colin et al. (2019). In such a model, the turbulent vertical diffusion formulation contains two additional term with respect to Eq. 2: a counter gradient term that allows the representation of fluxes due to non-local gradients and an explicit term for the entrainment at the PBL top, which is taken proportional to the surface buoyancy flux (Noh et al., 2003).

In SAM, the Smagorinsky closure is applied as a stationary version of the 1.5-order closure model (with turbulent kinetic energy, TKE or e, as a prognostic variable), where the vertical mixing coefficient is defined as in Eq. 4 with C_s being flow dependent and varying from 0.15 in unstable regions to 0.2 in the stably stratified region. $\overline{S}_\beta$ is evaluated as in WRF by using Eq 7, but with $Pr = 1$. The vertical mixing length is evaluated by using the Deardorff (1980) model:

$$l_v = \quad \Delta_z \qquad for\ N^2 \leq 0 \tag{12}$$

$$l_v = \quad min\Big[\Delta_z, 0.76\frac{e^{1/2}}{N}\Big] \qquad for\ N^2 > 0 \tag{13}$$

where e is the TKE and N is the local moist Brunt-Väisäla frequency (following M. F. Khairoutdinov and Randall (2003)). Since a prognostic equation for TKE is not activated in the Smagorinsky first order closure, the correction term for stable region in Eq. 13 is diagnosed from the mixing coefficient in the previous time step as $(0.76e^{1/2}/N) = \sqrt{0.76\ K_v/(C_k N)}$. Moreover, a minimum vertical mixing length is imposed as $l_v^{min} = 0.1\ \Delta_z$.

Grid anisotropy in SAM is taken into account by applying a correction factor to K_v as:

$$K_h = K_v \left(\frac{\Delta_x}{\Delta_z}\right)^2 \tag{14}$$

Therefore, the ratio between the horizontal and vertical mixing coefficient will be equivalent both for WRF and SAM ($K_h/K_v = (\Delta_x/\Delta_z)^2$) and the differences between the two schemes rely on the calculation of l_v, the values of C_s and the turbulent Pr number. The latter parameter is a prescribed constant value and it is fundamental not only because it is used in the mixing length calculation, but also because scalar diffusivity coefficients are simply obtained by dividing the momentum eddy viscosity coefficient by the Pr number. This is valid both for SAM and WRF models. Therefore, at similar values of eddy viscosity, smaller Pr numbers will cause larger scalar diffusivity.

SAM, instead of WRF, has no options for the enhancement of mixing in the PBL by non-local gradients. However, we decide to leave the PBL parametrization in WRF, since Tompkins and Semie (2017) demonstrated that convective organization is reached with or without the PBL parametrization when using the 3D Smagorinsky closure.

2.2 Simulations setup

All simulations are performed over a doubly periodic domain with a size of 768 x 768 km^2. The domain central latitude is set to zero. We set similar stretched vertical grids with 64 levels for both SAM and WRF: the first level is at about 25 m and grid spacing gradually increases from 50 m near the ground to 500 m above 5 km. Then it increases again from 500 m to 1 km above 20 km. A rigid lid is present at the top at about 27 km. To prevent unphysical wave reflection on the upper boundary, both WRF and SAM simulations have a sponge layer with traditional Rayleigh damping starting at the upper third of model domain. At the bottom there is an oceanic surface with a constant surface temperature of 302 K and the surface pressure is set to 1015 hPa. There is no background wind and the Coriolis parameter is set to zero. All simulations are run with fully interactive radiation and a diurnal cycle. Output fields are stored each hour.

SAM and WRF large domain simulations are initialized from the equilibrium sounding of a corresponding smaller domain RCE simulation (averaging over the last 20 days). The final RCE equilibrium reached by the small simulations presents some differences between SAM and WRF, even though they start from similar initial profiles. In particular, the WRF profile is moister and warmer than that of SAM and there is a lower Convective Available Potential Energy (CAPE) is present (see supplementary Fig S1 and S2). Similar differences between SAM-CRM and WRF-CRM model were found in RCEMIP project (Wing et al., 2020, , see their Figures 7g and 8g). Different initial conditions may strongly influence the sub cloud layer properties and CSA as demonstrated by (Cerlini et al., 2023). Further details about smaller domain simulations can be found in Supplementary Text S1.

Simulations are divided into three groups: main experiments, sensitivity experiments to initial conditions, sensitivity experiments to Pr number and sensitivity experiments to horizontal resolution. All experiments are listed in Table 3.

Table 3. List of experiments

Exp	Δ_x	Turbulence / Initial conditions	Days
Main			
WRF	3 km	Smag-default	100
SAM	3 km	Smag-default	100
WRF0	3 km	Smag-C_s=0	100
SAM0	3 km	Smag-C_s=0	100
Sensitivity to initial conditions			
WRFs	3 km	Smag-default / inital RCE profile from SAM	25
WRF0s	3 km	Smag-C_s=0 / inital RCE profile from SAM	25
Sensitivity to Pr number			
WRFPr1	3 km	Smag-default, Pr=1	100
SAMPr03	3 km	Smag-default, Pr=1/3	100
Sensitivity to horizontal grid resolution			
WRFh	1 km	Smag-default	45
WRF3h	1 km	3*Smag-default	30
SAMh	1 km	Smag-default	45
SAM3h	1 km	3*Smag-default, Pr=1/3	30

The main experiments are performed with a horizontal grid resolution of 3 km. They compare the standard version of the model (standard Smagorinsky and standard numerics) with the version of the model obtained by switching off the Smagorinsky turbulence model. This is obtained by imposing $C_s = 0$ in both SAM and WRF. While in SAM this corresponds to switching off completely the physical mixing (since a minimum coefficient is set on the mixing length prior to the mixing coefficient calculation), in WRF a small constant background mixing is left (see Eq. 8 and 10). The main experiments are run for at least 100 days and output fields are stored every hour. In the following, the first three letters of the simulation name represent the model name (e.g SAM, WRF), while the number 0 is appended to simulations with $C_s = 0$ (e.g. SAM0, WRF0).

Updraft entrainment and dilution is influenced not only by the mixing coefficient and the turbulence model but also by the properties of environmental (entrained) air. Therefore we perform an initial conditions sensitivity experiment, by initializing WRF and WRF0 simulations from the same initial conditions of SAM. Such simulation will be named WRFs and WRF0s. This is to prove the robustness of our results with respect to initial conditions.

One way to reduce the numerical mixing inherent to discretization schemes is to use a finer grid resolution. Therefore, the grid resolution sensitivity experiments are designed to investigate the impact of a finer horizontal resolution (1 km) on physical and numerical mixing. Two different high-resolution simulations of WRF are run: WRFh, which is the same as WRF, but with a resolution of 1 km; WRF3h, which is as WRFh, but the Smagorinsky constant is increased by three times. The same experiments are repeated for the SAM model: SAMh, which is the same as SAM, but with a resolution of 1 km; and SAM3h, where the resolution is 1 km, the Smagorinsky constant is increased by a factor of 3 and the Pr is reduced to 1/3 as the WRF value. To obtain a stable solution for the SAM3h experiment, we had to decrease the time step from 10 s to 5 s. In the following, simulations with 1 km resolution have a small "h" in the simulation name

(WRFh, WRF3h, SAMh, SAM3h). High-resolution simulations are run for at least 30 days and output fields are stored every hour.

3 Results

3.1 Convective aggregation state

Figure 1 shows the 2D snapshots of Outgoing Longwave Radiation (OLR) for the main experiments after 100 days. Convective self-aggregation occurs in WRF, SAM and SAM0: a small circular moist patch with deep convective activity (OLR < 120 W m^{-2}) of diameter around 200 km is surrounded by a larger and very dry region with suppressed convective activity (OLR > 280 W m^{-2}). In WRF0, on the other hand, convective activity is homogeneously distributed across the domain without the formation of extremely dry regions (Fig 1c).

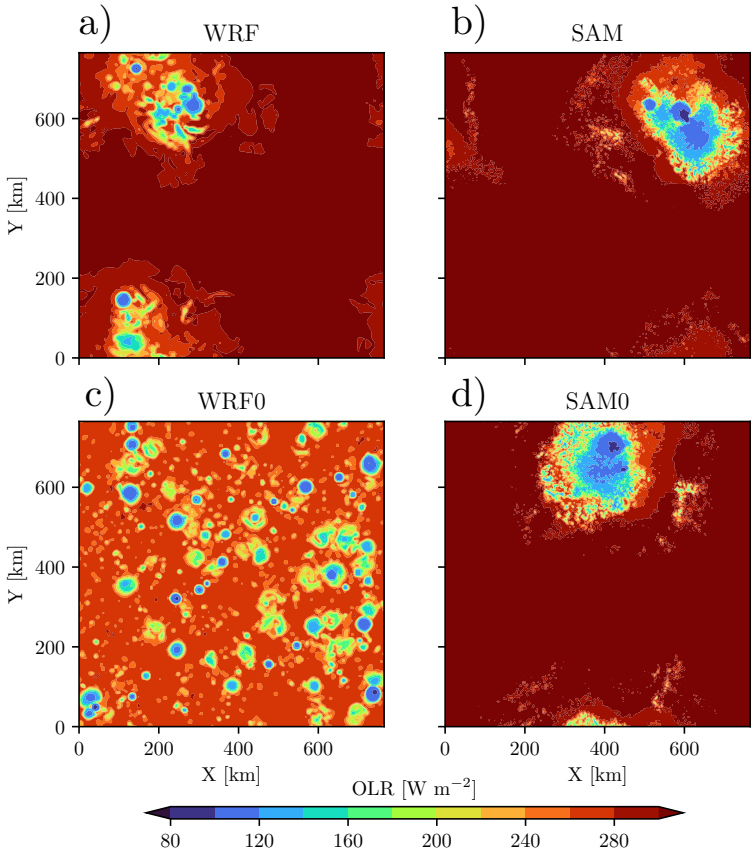

Figure 1. OLR instantaneous snapshots at midnight after 100 days for a) WRF, b) SAM, c) WRF0 and d) SAM0.

The aggregated simulations with active SGS mixing, SAM and WRF, show a similar temporal evolution of domain-average OLR, which increases by almost 50 W m^{-2} from the beginning of the simulation, reaching a stable value after 40 days. SAM0 shows the same increase but with a slower rate and a stable average OLR is reached after 60 days. WRF0 shows the same initial value of domain-average OLR throughout the simulation period.

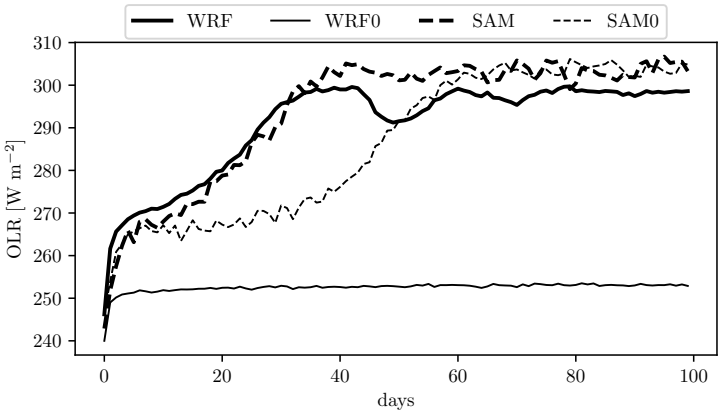

Figure 2. Domain averaged OLR time evolution for the main experiments.

Therefore, the reduction of horizontal diffusion in WRF is found to prevent CSA, as demonstrated by Tompkins and Semie (2017). The same cannot be said for SAM, confirming the previous results of C. J. Muller and Held (2012). SAM0 simulation demonstrates that the removal of turbulent mixing in SAM model, slows down the aggregation process, without preventing it. It is important to note that to characterize the effective slow down of aggregation caused by mixing, we should have run an ensemble of RCE simulations to take account for the stochastic variability of convective self-aggregation. Therefore, our interpretation of the role of mixing will focus on the triggering phase of CSA (the first 10 days) and only on whether a model exhibits or not a final aggregated state, rather than focusing on its degree of organization or its temporal evolution.

Figure 3 shows the initial (0-5 days, black lines) and final (last 10 days, red lines) profiles of temperature and relative humidity in the main experiments. Initially SAM has a lower temperature throughout the troposphere. However, after aggregation, the temperature profile reaches values comparable to WRF. SAM0 is not shown in Figure 3a since as no differences are found with respect to SAM. The increase in temperature in WRF with aggregation is smaller relatively to that of SAM, but it is still evident. WRF0 shows no changes with respect to the initial profile in WRF and is therefore not shown in Figure 3a. In the initial phase, the lower troposphere (below 6 km) is moister in WRF than in SAM and SAM0. No significant difference in relative humidity is found between SAM and SAM0, while the opposite is true for WRF and WRF0. Over the lower troposphere, WRF0 shows a very moist and well mixed profile with respect to WRF. This profile remain stable throughout the simulation period. The upper troposphere (above 6 km) of aggregated simulation (WRF, SAM, SAM0) is drier with respect to WRF0 in the initial stages and shows similar values even comparing different models. After aggregation, the domain dries out and similar profiles of RH are observed in WRF, SAM and SAM0.

The dryness of the upper free troposphere is the only factor common to the aggregated simulations with both models. This factor is already present in the early stages of the simulation as shown in Figure 3b even if the different models starts with different temperature and different lower tropospheric relative humidity profiles. The initial drying of the free troposphere is essential for CSA (B. Yang & Tan, 2020; Shamekh et al., 2020; Yanase et al., 2022), since it allows a more efficient radiative cooling of the boundary layer in the dry regions and the onset of a shallow circulation that transports MSE from dry to moist regions (upgradient), contributing positively to CSA. This drying has to be caused by a relatively fast and efficient process which is acting on the triggering phase of CSA, which is considered here to occur during the first 5 days. In order to better characterize this dry perturbation we will analyze the horizontal variability of con-

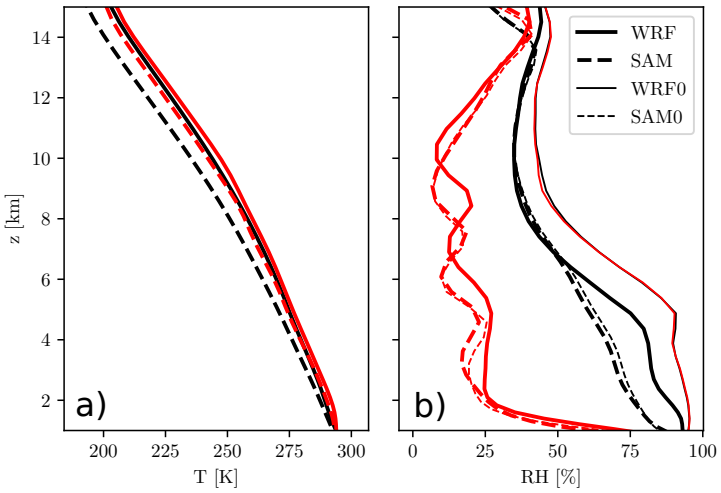

Figure 3. Vertical profiles of a) absolute temperature and b) relative humidity for the main experiments. Black lines show the average on the first 5 days, while red lines show the average over the last 10 days. WRF0 and SAM0 temperature profiles are not reported in a), since in the initial stage they are identical to WRF and SAM profiles, respectively. In the final stages, WRF0 does not show any change, while SAM0 has the same profile as SAM.

vection through the energy spectra (Section 3.2) and then focus on the physical processes responsible for creating such a perturbation (Section 3.3).

We obtain contrasting results between SAM and WRF models by switching off the SGS turbulence model. We hypothesize that this difference rely on the different implicit numerical mixing between the two models. This hypothesis will be demonstrated later by the sensitivity experiments performed on finer horizontal resolution.

3.2 Energy spectra and horizontal variability of convection

Energy spectra of quantities such as kinetic energy (KE) and vertical velocity can be used as a measure of the model's ability to reproduce the correct energy statistics (Skamarock, 2004) and to verify the model dynamics against the observations as reported by Nastrom and Gage (1985) and Lindborg (1999). This is especially true in Convective Self-Aggregation studies, where the horizontal variability of water vapor and atmospheric motion play a fundamental role. For example, Yanase et al. (2022) analyzed horizontal spectra of specific humidity, horizontal and vertical velocity at 2.5 km height, as obtained by idealized RCE simulations performed at various domain sizes with the SCALE-RM model (Nishizawa et al., 2015). They found that the larger the domain size, the larger the power of specific humidity (especially in the lower FT) that can be stored at longer wavelengths and, therefore, the larger its horizontal variance. Moreover, they also observed that the occurrence of aggregation corresponds to a transition from a state in which energy is primarily transported by small vertical motions to a state in which energy from large-scale horizontal motion dominates. This result highlights the importance of studying how small vertical motions (convective updrafts) are represented by different models as they are very sensitive to mixing processes (Tompkins & Semie, 2017). Also Janssens et al. (2022) underlined the importance of studying the interaction between numerical and modeling errors (generated by discretization schemes and SGS models) with the resolved large-scale dynamics of RCE in the CRM. In a preliminary analysis of the Power Spectral Density (PSD) of Total Water Path (TWP) and the vertical velocity at 500 hPa of 5 RCEMIP models, they showed that at grid spacing coarser than 1 km, very different energy was

contained at shorter wavelengths among different models. In particular, models with more energetic small-scale vertical motions contains more variance in water vapor at larger scales.

We compute energy spectra for horizontal Kinetic Energy (KE), vertical velocity (w), and virtual potential temperature perturbation ($\theta_v^{'}$ where $\theta_v = \theta(1 + 0.608q_v)$) both in the free troposphere (averaging from 3 km to 10 km) and in the boundary layer (averaging up to 2 km). Then we also compute energy spectra for the Total Water Path (TWP, calculated as the sum of all water species), integrating either over the whole column or over the boundary layer (from 0 to 2 km). While KE and w variables are important to understand the horizontal variability of atmospheric motions, $\theta_v^{'}$ and TWP give us a measure of buoyancy and humidity fluctuations. The results for the free troposphere (and the whole column TWP) are shown in Figure 4, while the boundary layer calculation is reported in Supplementary Figure S3. The horizontal one-dimensional PSD of each variable is obtained following the procedure of D. Durran et al. (2017). The PSD is then multiplied by the corresponding wavenumber in order to have a direct correspondence between the variance of the variables and the areas underneath the reported spectrum curves. All the spectrum figures contain two reference lines (dashed gray lines): the vertical line indicates wavelengths equal to 12 km which is taken as an indication of the effective resolution of the model (4Δx, D. R. Durran, 2010); the oblique line shows the $k^{-5/3}$ power law which is commonly observed where there is a turbulent energy cascade. Lai and Waite (2023) found that RCE simulations with the WRF model at 4 km horizontal resolution can show the -5/3 power low in the KE spectrum in the upper troposphere. However, from their spectral budget analysis, they found that this spectrum to be generated by a balance between forcing by buoyancy flux and removal by vertical energy flux, instead of a turbulent cascade (where nonlinear advective transfer is the main contribution to the budget analysis).

There are two main differences between the kinetic energy distribution of SAM and WRF as shown in Figure 4a and 4b: 1) SAM atmospheric motions, both in the vertical and in the horizontal, contain more energy across all scales; 2) the difference between kinetic energy spectra increases at smaller scales where WRF is found to damp small fluctuations (wavelengths less than $4\Delta x$), whereas in SAM small horizontal and vertical motions shows a large small-scale variance in the total kinetic energy. These two diverging behavior of kinetic energy reflect different modeling approaches at short wavelengths: WRF uses explicit filters to add scale-selective dissipation and damp the shortest wavelengths which are not well resolved by the model grid, while SAM does not apply any explicit scale-selective filter allowing a larger energy input at the smallest resolvable scales.

One interesting aspect is that the decrease of turbulent mixing in SAM0 did not significantly alter the kinetic energy spectrum both in the horizontal and in the vertical. This may be an indication that in SAM, at grid resolution larger than 1 km, the energy dissipation is controlled mainly by the numerical discretization.

The development of CSA in WRF and SAM simulations causes similar changes to the distribution of energy in both WRF and SAM. With CSA, the spectrum of horizontal KE and vertical velocity becomes more dominated by large-scale motions rather than small-scale motions as found in the non-aggregated case (Figure 4a and 4b). Such an increase of large-scale variance is not observed in the WRF0 simulation, whose spectrum remains constant throughout the simulation. In particular, WRF0 is characterized by smaller and less energetic horizontal and vertical motions already from the beginning of the simulation. Indeed an increase of energy at the smallest resolvable scales is evident in 4a.

The diverging behavior at small scales between SAM and WRF is also visible in the spectra of TWP and $\theta_v^{'}$ as shown in Figures 4c and 4d. Larger humidity and buoyancy fluctuations are present in SAM at small scales. This was evident also by the large presence of small cloud structures in SAM simulations as shown by the OLR snapshots (e.g. Figure 1a and 1b). The energy peak of TWP for WRF is found at wavelengths around 20 km. For SAM, this peak is lower and it is found at slightly larger wavelengths (about

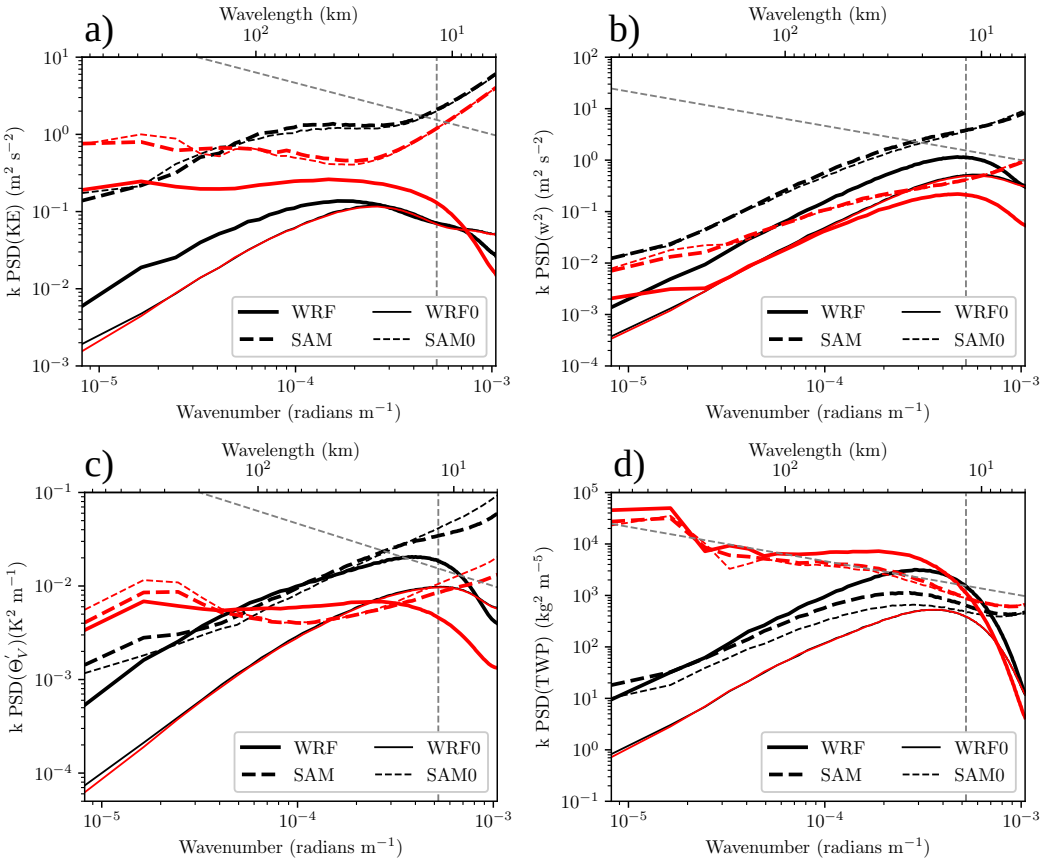

Figure 4. Power spectral densities of a) horizontal Kinetic Energy (KE), (b) vertical velocity (w), (c) perturbation virtual potential temperature ($\theta_v^{'}$), averaged over the free troposphere (between 3 and 10 km) and d) total water path (TWP) averaged over the whole column. The reported values are time-averaged in the initial 5 days of simulation (black lines) and the last 10 days (red lines). The PSD is multiplied by the corresponding wavenumber to have a direct correspondence between the variance of the variables and the areas underneath the curves. The oblique gray dashed line represents the $k^{-5/3}$ power law, while the vertical gray dashed line marks the effective resolution of the model, taken as $4\Delta x$.

30 km). However, the TWP spectrum is quite flat from wavelength smaller than 30 km, indicating that strong updrafts and cloud structures in SAM can be found at very different scales. Instead, in WRF, as shown also in Figure 1a, small deep convective cores and clouds are rare.

When CSA occurs (red lines in Figures 4c and 4d), there is an increase in humidity and virtual potential temperature variance at large scales. Such increase is very large for TWP. The same production of mesoscale humidity variance was observed by Yanase et al. (2022) andJanssens et al. (2022) in the aggregation of deep convection in several models and by C. Bretherton and Blossey (2017) in the mesoscale aggregation of shallow cumulus (see their Figure 16). The most prominent change of SAM and WRF with the reduction of turbulent mixing is evident in the initial stages in the variability of TWP, as shown in Figure 4d. Lower horizontal turbulent mixing in SAM0 and WRF0 causes a smaller variance of TWP across all scales. In this way, smaller perturbations of humidity will delay the onset of aggregation (as in SAM0), or prevent it (as in WRF0). The reduction of humidity variance in WRF is greater than in SAM.

The reduction in free tropospheric moisture variance with decreased horizontal mixing is well correlated with a more active boundary layer in both SAM and WRF as seen in the vertical velocity spectrum in Fig. S3b.

3.3 FMSE variance budget

The time evolution of CSA is characterized by an increase in the Frozen Moist Static Energy (FMSE) variance, where FMSE is defined as:

$$h = c_p T + gz + L_v q_v - L_f q_i \tag{15}$$

where c_P is the specific heat of dry air, T is the air temperature, g is gravitational acceleration, z is the height above the surface, L_v is the latent heat of vaporization, q_v is the specific humidity with respect to water vapor, L_f is the latent heat of fusion, and q_i is the specific humidity with respect to ice condensates. The evolution of its horizontal spatial variance, $\widehat{h}'^2$, is shown in Figure 5a for the main experiments. (For each quantity x, we denote "$\widehat{x}$" as its density-weighted vertical integral $\int_0^{z_{top}} x\rho dz$. The horizontal domain mean of x is instead denoted as $\{x\}$ and the anomaly as x'.). WRF and SAM exhibit a similar exponential growth of variance and they reach a stable equilibrium state after 40 days. The final variance values are also very similar between the two models. In order to study the feedback that cause the increase of the FMSE variance, we perform the budget analysis according to the evolution equation of $\widehat{h}'^2$ by Wing and Emanuel (2014):

$$\frac{1}{2}\frac{\partial \widehat{h}'^2}{\partial t} = SEF'\widehat{h}' + NetSW'\widehat{h}' + NetLW'\widehat{h}' - \widehat{h}'\nabla_h \cdot \widehat{\vec{\mathbf{u}}h} \tag{16}$$

where SEF are the total surface enthalpy fluxes (the sum of the latent and the sensible heat flux), NetSW and NetLW are the column shortwave and longwave radiative flux convergence, and $\nabla_h \cdot \widehat{\vec{\mathbf{u}}h}$ is the horizontal divergence of the vertically integrated flux of h, which is evaluated as a residual of the remaining terms.

Figure 5b, 5c, 5d and 5e show the contribution of longwave radiation, shortwave radiation, surface fluxes and advection processes to the increase in FMSE variance in the main experiments.

Radiative processes have very similar magnitude and evolution between SAM and WRF: they contribute positively to self-aggregation throughout the simulation time. In particular, longwave feedback are the drivers of CSA in the first stages up to 10 days, with WRF having higher correlations than SAM. After 10-20 days, longwave and shortwave feedback have similar magnitudes and remain almost constant, indicating that they

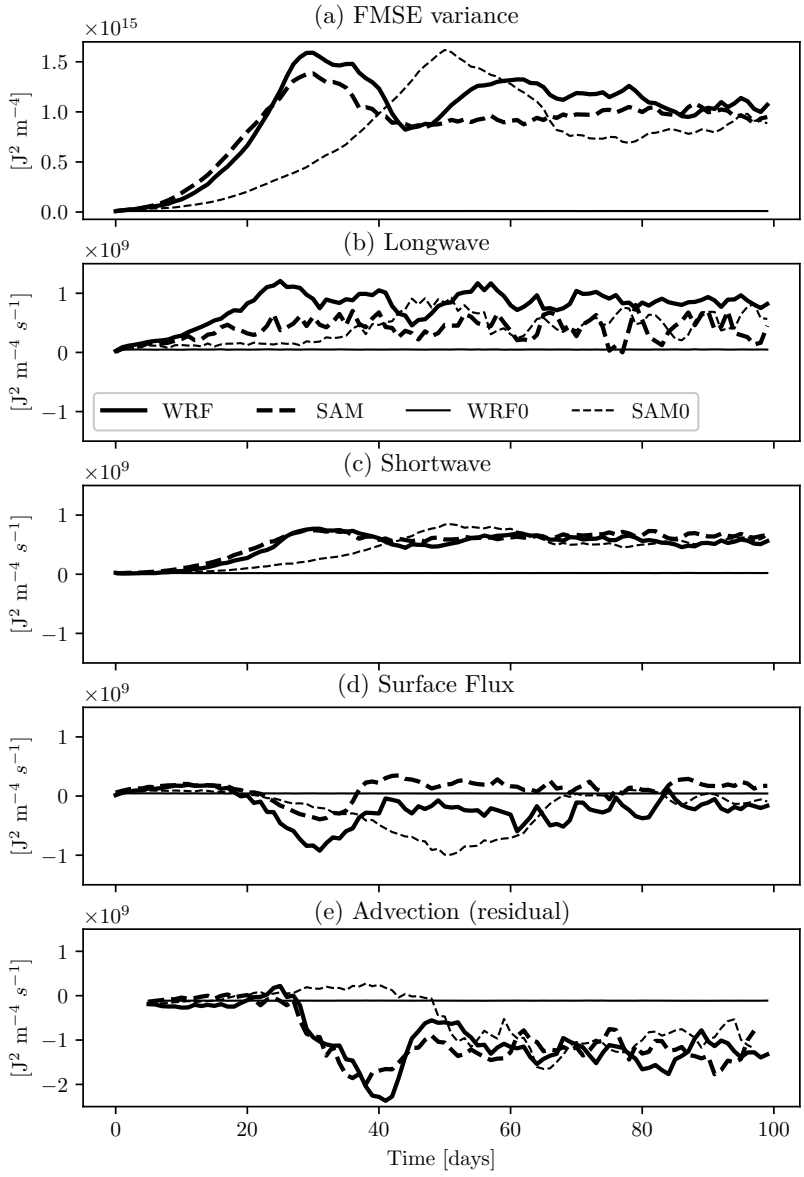

Figure 5. The budget of FMSE variance for all 100 simulations including: a) time evolution of the domain mean spatial variance of the vertical-integrated Frozen Moist Static Energy (FMSE) (J^2/m^4) for the main experiments; b), c) and d) and e) shows the contributions to the FMSE budget by longwave, shortwave, surface flux and advection (evaluated as a residual term), respectively. Each contribution is averaged daily and a 5-day running average is applied to the horizontal convergence term.

are responsible for maintaining CSA. Surface enthalpy flux contributions are positive up to 20 days for both SAM and WRF. However, in SAM they exert stronger positive feedback than in WRF, especially in the early stages where their magnitude is comparable with that of longwave radiative processes. After 20 days, the contribution of surface fluxes becomes negative, thereby opposing self-aggregation. Then, in SAM they return to beeing slightly positive, while in WRF they remain slightly negative. This is one of the few differences between WRF and SAM simulations, regarding this budget analysis. Advective contributions are counter to CSA in the early stages, but they become slightly positive in a time window of 10 days, which corresponds to the time when the convection starts to organize into a single cluster. This time window starts earlier in SAM than in WRF and overlaps with the time when the surface fluxes feedback becomes slightly negative. After the convective cluster has formed, the advective processes return to be negative, counteracting the CSA and the radiative feedback that sustain it.

From the above FMSE analysis, convective self-aggregation is primarily triggered by radiative and surface fluxes feedback. However the contribution of SGS turbulent mixing is not taken into account in Equation 16. By using Eq. 2 for modeling turbulent diffusion of FMSE, one can add the SGS mixing contribution to the FMSE variance budget as follow:

$$\frac{1}{2}\frac{\partial \widehat{h}'^2}{\partial t} = SEF'\widehat{h}' + NetSW'\widehat{h}' + NetLW'\widehat{h}' - \widehat{h}'\nabla_h \cdot \widehat{\vec{\mathbf{u}}h} + \widehat{h}'\nabla_h \cdot (-\frac{\widehat{K_h \nabla h}}{Pr}) \qquad (17)$$

Figure 6 offer a zoom of Figure 5 during the first 10 days, including also the effect of SGS mixing. The increase in the FMSE variance in Figure 6a is quite similar between WRF and SAM, while it is slower in SAM0 and absent in WRF0. This correlates with the total diabatic feedback, as they show similar increase in magnitude for SAM and WRF, while a slower increase in SAM0 and no increase at all for WRF0. Surprisingly, the SGS mixing term shows much larger positive correlations than the total diabatic feedback in the very early stages for SAM and WRF, implying that it strongly favors CSA and it cannot be neglected at such horizontal resolution. Looking only at SAM and WRF simulation, this result implies that a strong cooperation between SGS mixing and diabatic feedback is necessary to start the diabatic feedback loop which is then responsible for the expansion and maintenance of dry patches.

However, switching off such feedback in SAM0 does not prevent a constant increase in the magnitude of diabatic feedback, while it does in WRF0 where the amplitude of diabatic feedback remain constant. We hypothesized that this behavior is related to the implicit numerical entrainment which is present in SAM, when used at coarse resolutions. We will test this hypothesis by looking at the FMSE budget at finer resolution with different explicit and implicit mixing.

3.4 Triggering mechanism of CSA

From the analysis of the horizontal variability of convection and the FMSE budget, it is clear that mixing processes are fundamental for triggering CSA. In particular, we argue that the radiative feedback loop which is responsible for the initial formation and the expansion of dry patches in the very initial stages, is initiated by an indirect path through the environment for convection instead of the direct path trough the WTG velocity. This is consistent with previous findings by Yanase et al. (2022). Following the work by Tompkins and Semie (2017), we suggest that the free-tropospheric drying and the associated radiative subsidence are strictly dependent on lateral mixing and updraft dilution. Models with an efficient mixing, either numerical or explicit, will allow for greater large-scale variability of convection and therefore greater dry perturbations over the free troposphere. Only when a sufficiently strong dry perturbation is established by updraft dilution and reduced convective heating and moistening, then a strong boundary layer radiative cooling in dry region is able to start the upgradient MSE shallow circulation

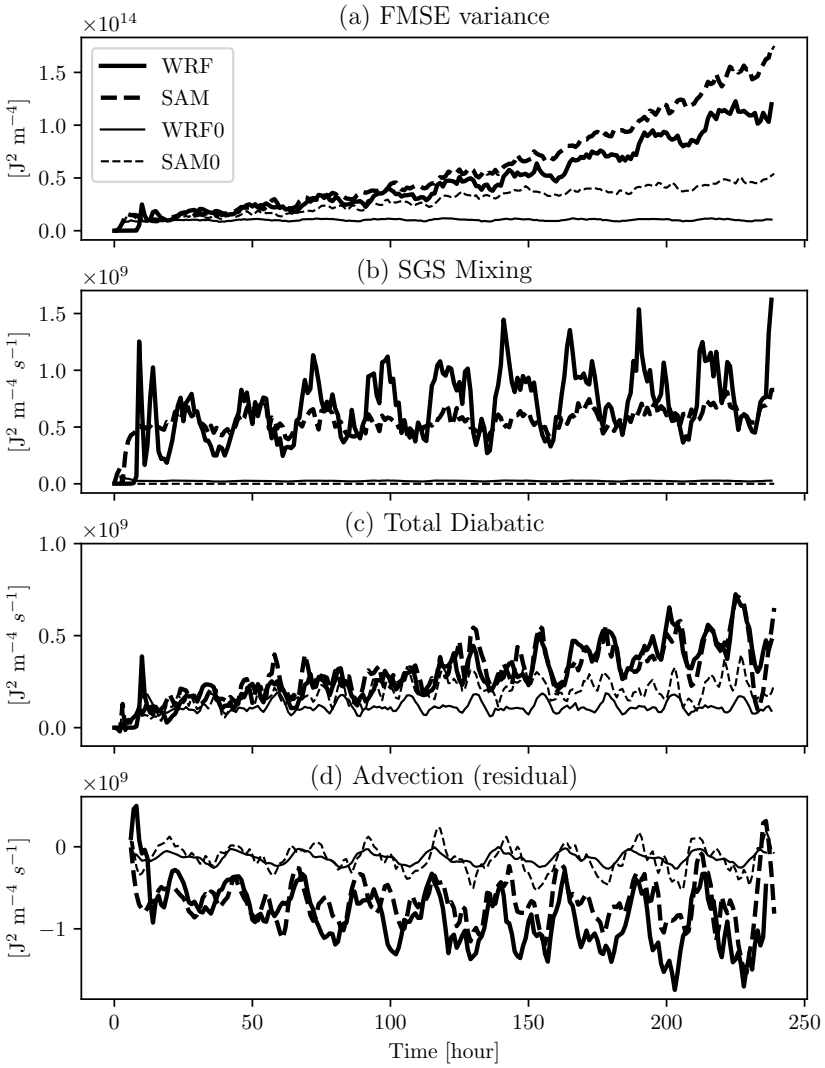

Figure 6. The budget of FMSE variance for the first 10 days including: a) time evolution of the domain mean spatial variance of the vertical-integrated Frozen Moist Static Energy (FMSE) (J^2/m^4) for the main experiments; b), c) and d) and e) shows the contributions to the FMSE budget by SGS mixing, diabatic feedback (longwave, shortwave and surface flux) and advection (evaluated as a residual term), respectively. Each contribution has an hourly time-step and a 6-hour running average is applied to the horizontal convergence term.

and expand dry patches, as also found by Shamekh et al. (2020). Figure 7 shows respectively radiative cooling, static stability, cloud fraction, radiative velocity (calculated as the ratio between radiative cooling and static stability following Bony et al. (2016)) and the actual velocity in the driest regions (the lowest quartile of block-averaged Column Relative Humidity, CRH) averaged over the first 5 days. The strongest differences in the radiative cooling profiles are evident in the boundary layer below 2 km (see Figure 7a). Simulations with convective self-aggregation shows an average cooling of -1.5 K/day over the boundary layer with a peak at 1 km corresponding to the maximum low-level cloud amount (see Figure 7c). However, this cooling is not present in WRF0. The reason behind the absence of such cooling cannot be traced back to the decrease of radiative subsidence, since Figure 7d shows that between 2 and 10 km the radiative velocity between WRF and WRF0 is quite similar. Instead this difference has to be related to the high amount of the mid-level clouds (Figure 7c) and the positive low-level actual velocity (Figure 7e) in the driest region, which implies that convection is able to penetrate into the free troposphere of dry regions and destroy any nascent dry perturbation.

Although the WTG path, radiative velocity and clear-sky convergence may be useful for explaining different anvil cloud fraction, cloud top and temperature, Figure 7 shows that they cannot explain the different sensitivity of CSA in SAM and WRF to mixing processes. In fact, despite the different radiative cooling in the upper troposphere and the different static stability (Figures 7a and 7b), the WTG velocity, as diagnosed from the radiative cooling, is quite similar between SAM and WRF between 2 and 8 km. This is because the warmer atmosphere in WRF cause a larger radiative cooling which compensates for the greater static stability with respect to SAM. A similar effect was found also by Shamekh et al. (2020) by varying SST.

4 Sensitivity studies

4.1 Sensitivity to initial conditions

Entrainment and updraft dilution depend also on the ambient temperature and relative humidity. A drier atmosphere, especially in the lower troposphere such as that of SAM, would amplify the dilution effect. On the other hand, in warmer atmospheres, such as that of WRF, entrainment is more effective in reducing updraft buoyancy (Singh & O'Gorman, 2013). Different mixing efficiency due to different environment could lead to different thermal stratification (static stability). Through the Weak Temperature Gradient hypothesis this would directly impact the radiatively driven subsidence (and all the deep convective circulation in general), the clear-sky convergence and also the anvil cloud fraction (Bony et al., 2016) with possible consequences for convective self-aggregation. However, based on our previous results, we have shown that the free-tropospheric drying necessary to start the radiative feedback loop, is not directly caused by the WTG path, but by the initial dry perturbations set by mixing processes. Therefore we do not expect self-aggregation in WRF0 even if we start the model with a colder atmosphere and a drier lower troposphere.

Figure 8 further confirm our findings. Even by starting WRF and WRF0 by using SAM initial RCE profiles (respectively WRFs and WRF0s), the relative occurrence of convective-self aggregation in the two simulations is not changed. Indeed after 10 days, Figure 9 shows that the temperature and humidity profiles of WRFs and WRF0s are very close to their corresponding simulation initialized with warmer and moister atmospheres (WRF and WRF0). A small free tropospheric drying is evident in WRF0s (see Figure 9b), but this is not sufficient to start the radiative feedback loop.

The WRF model seems to be very efficient in moistening the lower troposphere with respect to SAM, even with a very small amount of mixing, as in WRF0s. This is mainly due to the convectively-induced moistening which is favored by a reduced updraft dilution, as denoted by the difference between WRFs and WRF0s in Figure 9b. Morevoer, it could also be related to the fact that SAM does not have a planetary boundary layer

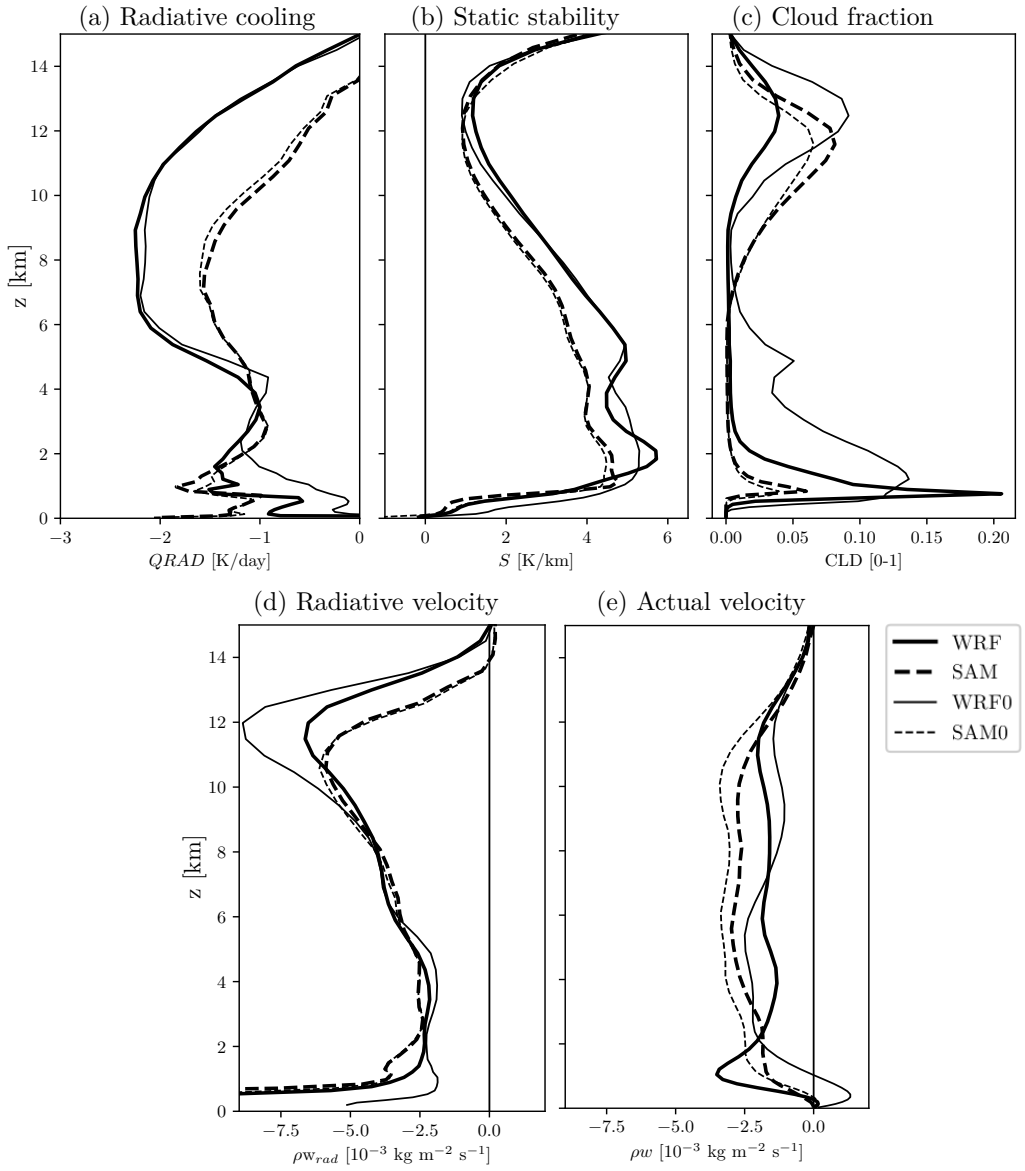

Figure 7. Vertical profiles of (a) radiative cooling, (b) static stability, (c) cloud fraction, (d) radiative velocity (obtained as the ratio between radiative cooling and static stability), (e) actual velocity. All quantities are averaged over the first 5 days and over the driest regions. Following the approach by C. S. Bretherton et al. (2005), all quantities are sorted into four quartiles by the block-averaged Column Relative Humidity (CRH), computed by dividing the simulations domain into blocks with area of 96 km^2. Driest regions correspond to the lowest quartile.

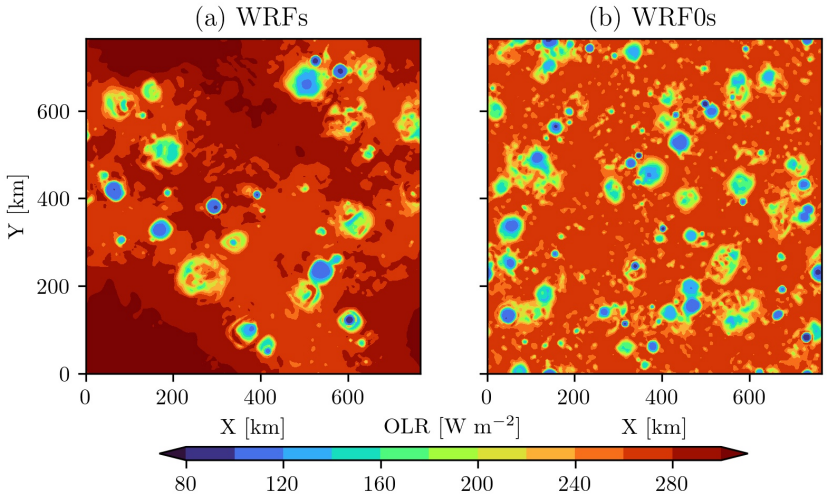

Figure 8. OLR instantaneous snapshots at midnight after 20 days for a) WRFs and b) WRF0s.

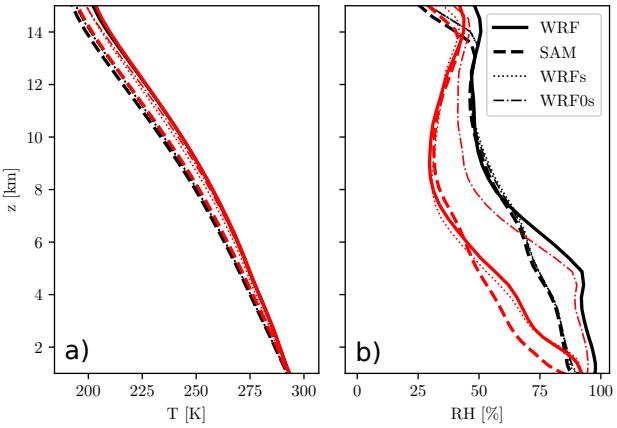

Figure 9. Vertical profiles of a) absolute temperature and b) relative humidity for the simulation WRF, SAM, WRFs and WRF0s. Black lines show the average on the first 6 hours in order to show the corresponding initial conditions between SAM, WRFs and WRF0s and their difference with respect to WRF. Red lines show the profiles averaged over day 10. After 10 days the profile of temperature and relative humidity of WRFs and WRF0s are very close to that of the respective simulations WRF and WRF0, indicating a small influence of initial conditions on the occurence of self-aggregation.

scheme, while WRF does. However, the impact of the planetary boundary layer scheme in WRF has already investigated by Tompkins and Semie (2017), and they found that including vertical mixing with a PBL scheme favors CSA. Therefore the results obtained for WRF0s should be conservative with respect to the choice of the PBL scheme.

Figure 10 shows the correspondent increase in diabatic feedback and SGS mixing feedback for WRFs with respect to WRF. Another difference is the strong peak observed in WRFs in the FMSE variance at 12 hours with respect to that of WRF. This peak is the consequence of a larger effective updraft dilution in dry regions in WRFs with respect to WRF. The reduction in the number of deep convective cores is reported in Supplementary Figure S4.

We conclude that the free-tropospheric drying caused by updraft dilution in WRF depends mainly on the SGS mixing and that a drier environment is not sufficient to allow convective self-aggregation to develop in the absence of lateral mixing. This necessary condition for CSA triggering is again shown in Figure 11a, where we highlight the difference in large-scale horizontal variability of convection between WRFs and WRF0s during the first 5 days.

Figure 12a shows the resulting differences in cloud fraction profiles. The most significant difference between WRF and WRFs is an increase in the height at which low-level cloud form and a decrease of the height of anvil clouds. WRF0s and WRFs generally show a larger anvil but they have same distribution of WRF and WRF0 in the lower troposphere. The decrease in anvil cloud height and their increase in coverage can be traced back to the colder atmosphere of WRFs and WRF0s in agreement with the study of Stauffer and Wing (2022), and it also partly explain the difference between SAM and WRF simulations. However, the large differences in upper tropospheric and low-level cloud cover profile between SAM and WRFs depend mainly on the microphysics scheme.

4.2 Sensitivity to Pr number

By default, the WRF and SAM models use different Pr numbers, equal to 1/3 for WRF and 1 for SAM. The Pr number is a fundamental constant in the calculation of the eddy viscosity and eddy diffusivity. First, it appears in the calculation of the resolved strain tensor (Equation 7) as a weighting factor in the reduction of mixing in very stable atmospheric conditions. Therefore, holding the resolved strain tensor and the buoyancy frequency constant (hence a constant Richardson number), the smaller the Pr number, the greater the reduction of mixing in a stable stratified state. Secondly, the eddy diffusivity is derived by dividing the eddy viscosity by the turbulent Pr number. Therefore a larger Pr number implies a smaller eddy diffusivity, at constant eddy viscosity.

Due to its influence in scalar mixing processes, we expect a large sensitivity of CSA to the Pr number. In particular, given Eq 16, the smaller the Pr number, the larger the contribution of SGS mixing in the increase of FMSE variance and the larger the moisture-convection feedback that allows free tropospheric drying.

Figure 13 shows the OLR field after 20 days. The onset of CSA is clearly visible in SAMPr03, while WRFPr1 shows no sign of CSA. Therefore, increasing the Pr number to 1 in WRF is enough to prevent CSA, as also found by Shi and Fan (2021) for the CM1 model. After 100 days, WRFPr1 exhibits always random convection like WRF0 and WRF0s, while SAMPr03 aggregated state is very similar to SAM and SAM0 simulations.

As expected, decreasing the Pr number in SAM increases the strength of SGS mixing and diabatic feedback as shown in Figure 10b and Figure 10c. This corresponds to a faster increase in the FMSE variance (Figure 10a).

The variability of the Total Water Path in SAMPr03 decreases at all scales (Figure 11b). However the large-scale variability remains always bigger than WRF0 and of the order of magnitude of that of SAM and WRF. The same cannot be said for WRFPr1 which instead exhibits a smaller large scale variability very similar to that of WRF0. The

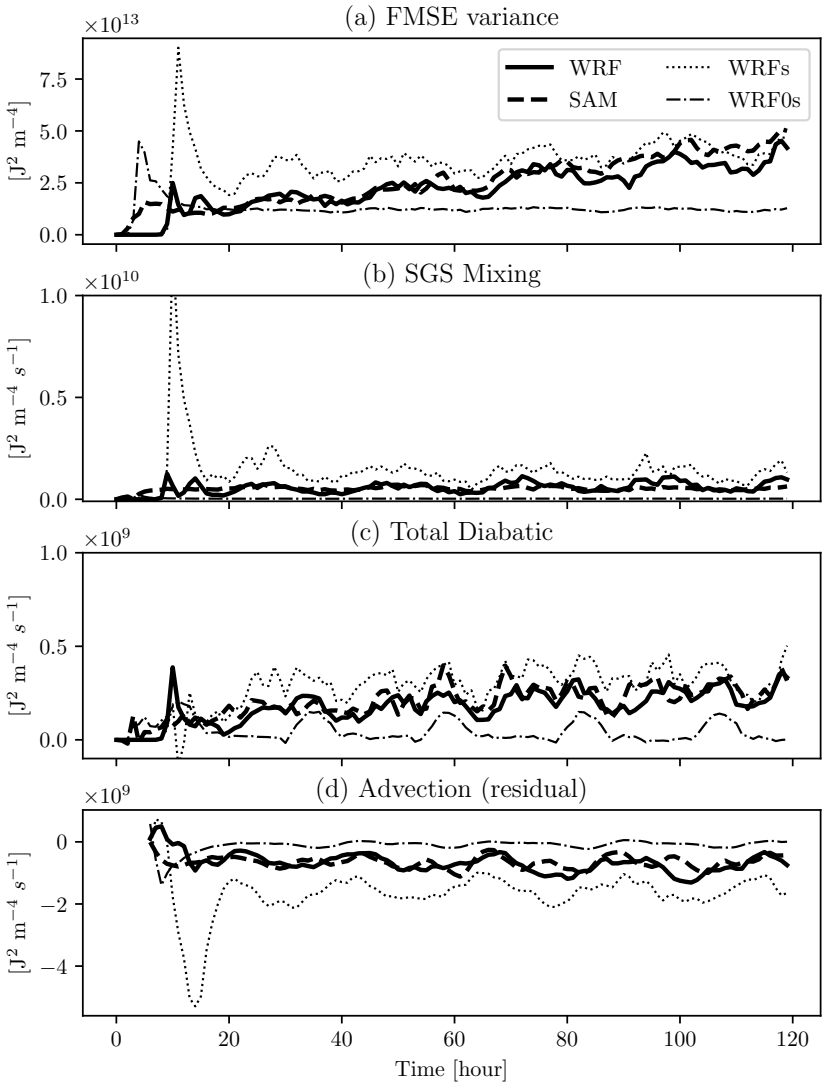

Figure 10. The budget of FMSE variance for the first 5 days including: a) time evolution of the domain mean spatial variance of the vertical-integrated Frozen Moist Static Energy (FMSE) (J^2/m^4) for the initial sensitivity experiments; b), c) and d) and e) shows the contributions to the FMSE budget by SGS mixing, diabatic feedback (longwave, shortwave and surface flux) and advection (evaluated as a residual term), respectively. Each contribution has an hourly time-step and a 6-hour running average is applied to the horizontal convergence term.

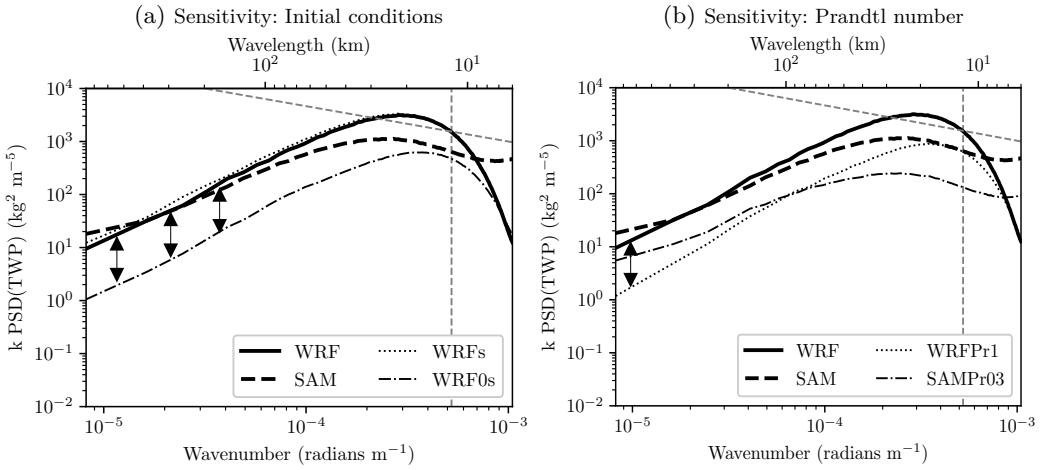

Figure 11. Power spectral densities of total water path (TWP) averaged over the whole column and over the first 5 days for a) sensitivity experiments on initial conditions, b) sensitivity experiments to Pr number. The PSD is multiplied by the corresponding wavenumber to have a direct correspondence between the variance of the variables and the areas underneath the curves. The oblique gray dashed line represents the $k^{-5/3}$ power law, while the vertical gray dashed line marks the effective resolution of the model, taken as $4\Delta x$.

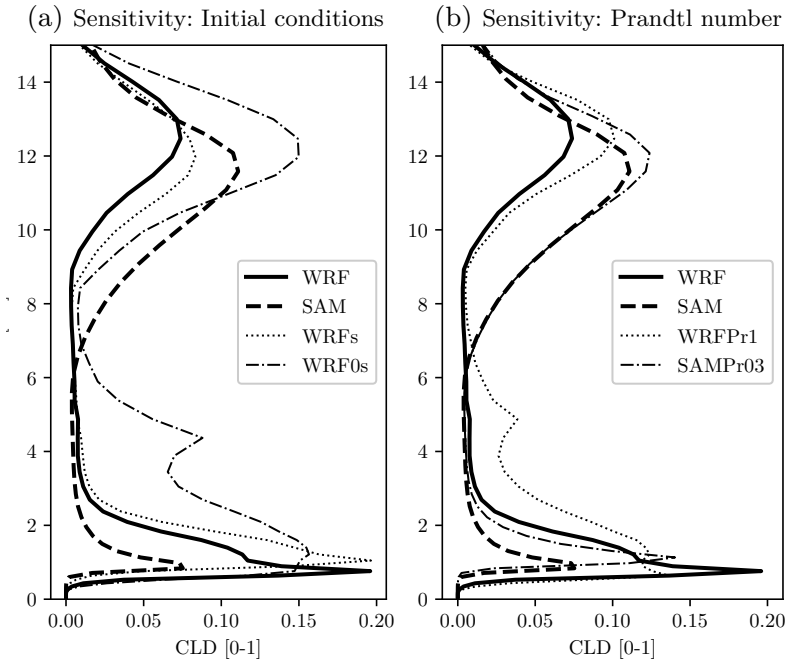

Figure 12. Vertical profiles of domain-mean cloud fraction avaraged over the first 5 days for a) sensitivity experiments on initial conditions, b) sensitivity experiments to Pr number.

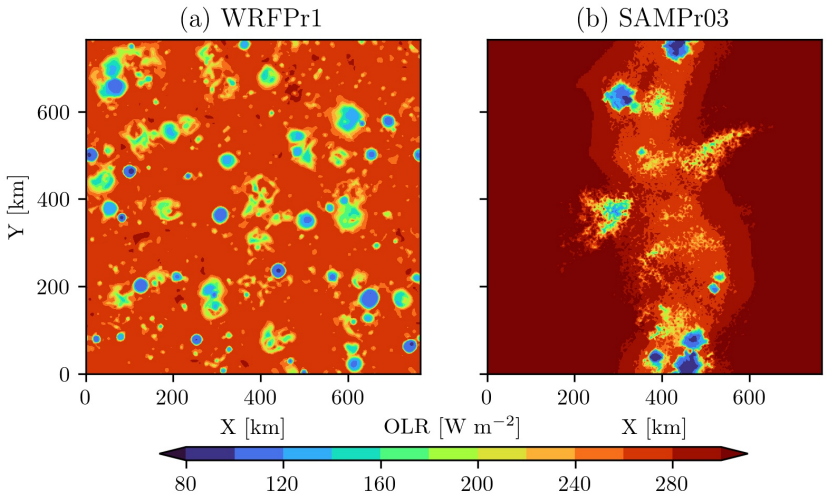

Figure 13. OLR instantaneous snapshots at midnight after 20 days for a) WRFPr1, b) SAMPr03.

similarity between WRF0 and WRFPr1, SAM and SAMPr03 can be seen also by looking at the relative humidity vertical profiles shown in Supplementary Figure S6.

Decreasing the Pr number in SAMPr03 doubles the average low-level cloud fraction, reaching values and depths more similar to that of WRF (see Figure 12b). The same increase is found also in the driest regions (not shown).

4.3 Sensitivity to horizontal resolution

In order to demonstrate that the SAM model has a large numerical mixing that makes CSA insensitive to SGS mixing at coarse resolution of 3 km, we run the main experiments WRF and SAM at finer resolution. We than reintroduce mixing explicitly, trough the SGS turbulence model, in order to obtain CSA with both models even at higher resolution. This demonstrates that the total amount of mixing, either implicit or explicit, regulates the large scale variability of convection and therefore the free-troposphere drying necessary to trigger CSA. A correct rescaling of mixing coefficient is needed if we want to maintain a constant large-scale variability.

Figure 15 shows the OLR snapshot for finer resolution simulations after 30 days. WRFh and SAMh simulations show no sign of CSA, although a larger scale variability of convection is evident in SAMh compare to WRFh (Figures 15a and b). Therefore reducing the mixing length by a factor 1/3 and reducing the numerical mixing is enough to prevent CSA for both models. CSA is restored by reintroducing explicit mixing in WRF3h (simply increasing by a factor 3 the Smagorinsky constant) and in SAM3h (by decreasing Pr number by a factor 3 and increasing the Smagorinsky constant by a factor 3, to have similar constant to WRF3h). We have not tried other combinations of Pr and C_s coefficient, so we cannot establish an absolute threshold for the onset of CSA.

WRF3h exhibits the strongest increase in FMSE variance, while SAM3h exhibits similar increase to those of SAM and WRF (Figure 16a). The effect of SGS mixing is larger in WRF3h compared to that of SAM3h, which is quite similar to that of all other simulations, except for SAMh, which has a very low correlation for this term. This is another signal of the larger contribution of numerical mixing in the SAM model. Indeed, at the same resolution and with same Pr numbers, WRF needs a much larger explicit mixing to trigger CSA.

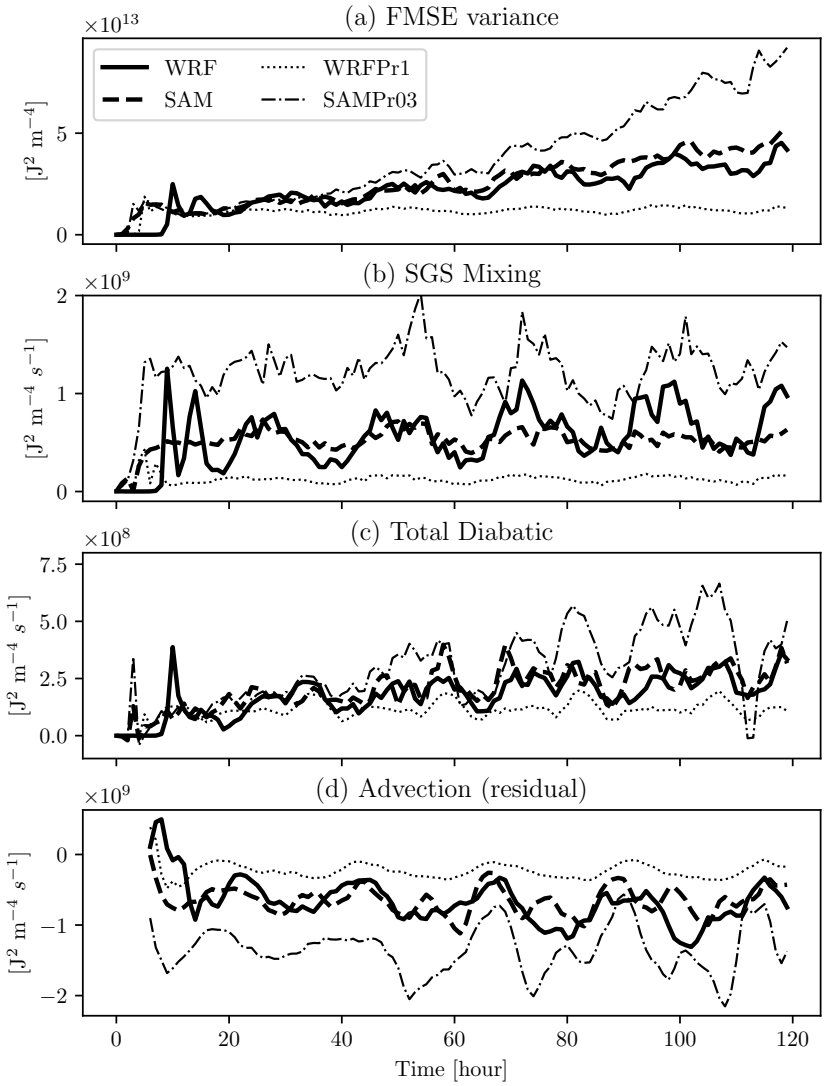

Figure 14. The budget of FMSE variance for the first 5 days including: a) time evolution of the domain mean spatial variance of the vertical-integrated Frozen Moist Static Energy (FMSE) (J^2/m^4) for the sensitivity to Pr number experiments; b), c) and d) and e) shows the contributions to the FMSE budget by SGS mixing, diabatic feedback (longwave, shortwave and surface flux) and advection (evaluated as a residual term), respectively. Each contribution has an hourly time-step and a 6-hour running average is applied to the horizontal convergence term.

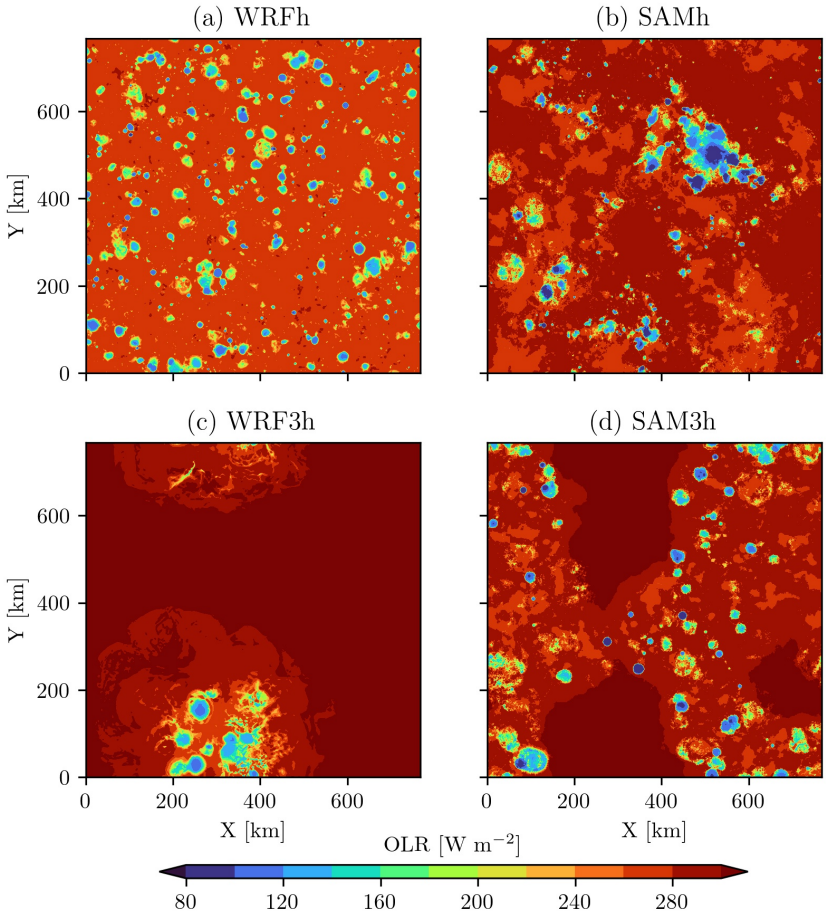

Figure 15. OLR instantaneous snapshots at midnight after 30 days for a) WRFh, b) SAMh, c) WRF3h, d) SAM3h

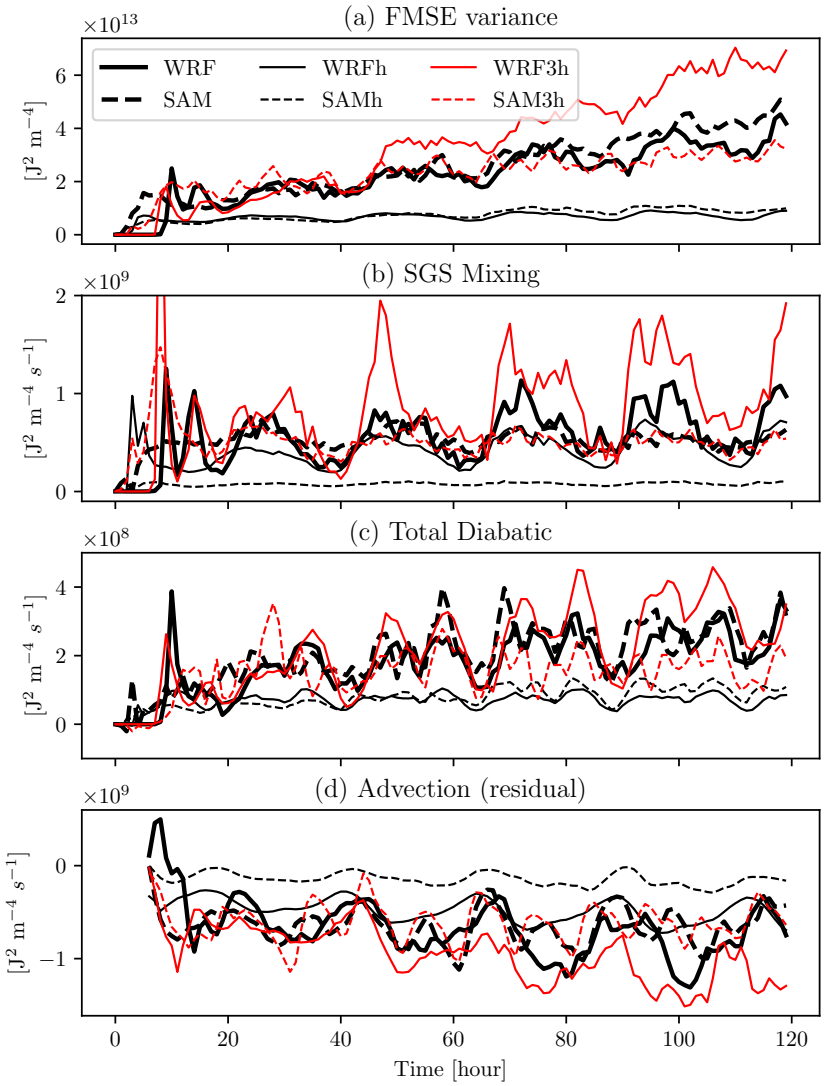

Figure 16. The budget of FMSE variance for the first 5 days including: a) time evolution of the domain mean spatial variance of the vertical-integrated Frozen Moist Static Energy (FMSE) (J^2/m^4) for the horizontal resolution sensitivity experiments; b), c) and d) and e) shows the contributions to the FMSE budget by SGS mixing, diabatic feedback (longwave, shortwave and surface flux) and advection (evaluated as a residual term), respectively. Each contribution has an hourly time-step and a 6-hour running average is applied to the horizontal convergence term.

In literature, the dependence of the occurrence of CSA with the horizontal grid resolution is commonly associated to the low-level cloud amount: the finer the resolution, the smaller the low-level cloud amount and the associated low-level radiative cooling which is necessary to start the shallow MSE upgradient circulation (C. J. Muller & Held, 2012; Yanase et al., 2020). Figure 17a shows that this dependence is found for the WRF model, since WRF and WRF3h have larger amount of low-level cloud fraction than WRFh. However, we recall that the main difference between WRF and WRF0 was not in the low-level cloud amount, but on the mid- and upper-level cloud amount in the driest regions (see Figure 7c). On the other hand, Figure 17a shows that the two simulations SAMh and SAM3h have similar low-level cloud fractions on average, demonstrating that we can obtain CSA even with a small amount of low-level clouds. From this analysis we conclude that the average amount of low-level clouds does not affecting the triggering phase of CSA, while it may be fundamental for its intensification and development.

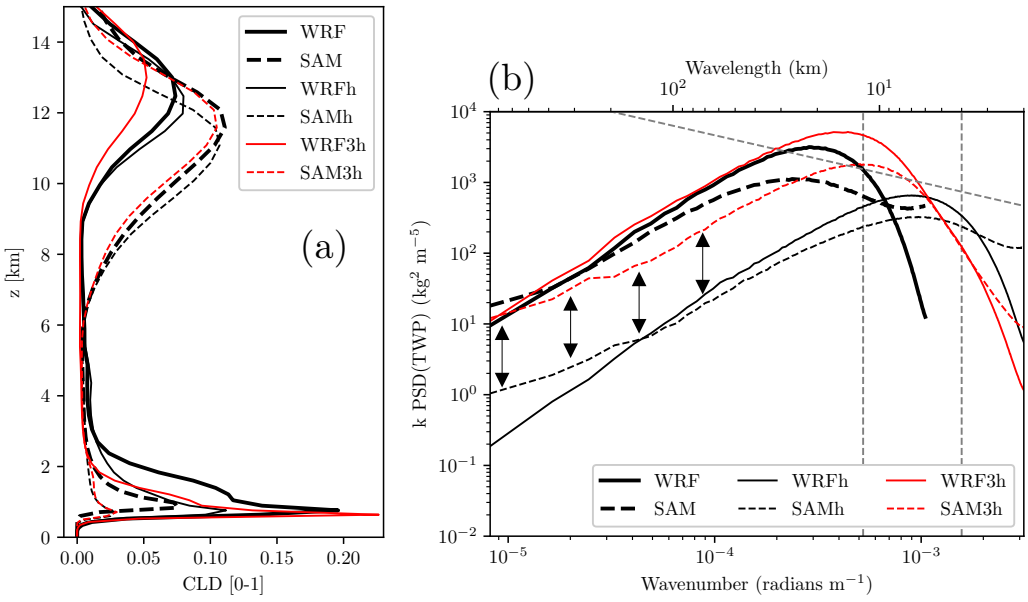

Figure 17. Sensitivity experiments to horizontal resolution: a) Vertical profiles of domain-mean cloud fraction avaraged over the first 5 days; b) Power spectral densities of total water path (TWP) averaged over the whole column and over the first 5 days. The PSD is multiplied by the corresponding wavenumber to have a direct correspondence between the variance of the variables and the areas underneath the curves. The oblique gray dashed line represents the $k^{-5/3}$ power law. The rightmost vertical gray dashed lines marks the effective resolution of the finer grid resolution model (4 km = $4\Delta x$). The leftmost vertical gray dashed lines marks the effective resolution of the coarser grid resolution model (12 km = $4\Delta x$).

The most important factor that binds all the aggregated simulations together in the very early stages of the simulation is the large-scale variability of the convection. This is shown in Figure 17b, where the difference in large-scale variance of TWP between the non-aggregated and aggregated cases is highlighted. It is interesting to note the larger large-scale variance of SAMh with respect to WRFh. This difference may be associated to the larger numerical mixing of SAM model with respect to the WRF model. This also

reflects the differences found in the horizontal variability of OLR between WRFh and SAMh (Figures 15a and 15b): WRFh has a more random and uniform convection, with smaller dry areas, while SAMh exhibit larger clusters of deep convective cores with larger dry areas.

Therefore, as found by Biagioli and Tompkins (2023) in its idealized model, by increasing the Smagorinsky constant, we enlarge the area of influence of each deep convective core and we increase their average size, by increasing also the mean distance between different cores and therefore the amplitude of dry perturbation introduced in the free troposphere. This allows to maintain the original updraft width even at a finer grid resolution and to restore CSA.

Such sensitivity experiments therefore confirm the hypothesis formulated by Windmiller and Craig (2019) that "large enough fluctuation in the humidity content has to be present for self-aggregation to start". We conclude that coarse resolutions will increase this initial fluctuation either through larger SGS mixing or numerical mixing.

5 Discussion

This study shows the relevant role of mixing and entrainment on the self-aggregation phenomenon. The level of mixing and entrainment reproduced by numerical simulation is provided by both the explicit turbulence model and the numerical dissipation. Accordingly, we have shown a strong sensitivity of CSA to the different turbulence models and spatial resolutions adopted in SAM and WRF atmospheric models. We try capture the essential aspects here.

On one hand, in the SAM model, a lower turbulent mixing coefficient, hence a weaker moisture-convection feedback or moisture-entrainment-convection feedback (Tompkins & Semie, 2017), does not affect the onset of CSA. Therefore, looking only at this model, modifying the sensitivity of convection to water vapor cannot by itself destabilize the RCE equilibrium, as suggested by Emanuel et al. (2014). On the other hand, in the WRF model, turbulent mixing appears to be a necessary condition for CSA to occur. This result is consistent with previous work by Tompkins and Semie (2017). Apparently, different results coming from different numerical experiments support two different roles of the moisture-convection feedback in CSA.

The two contrasting results can be reconciled by considering all scalar mixing processes either explicit (turbulence, hyperviscosity, or other explicit numerical filters) or implicit (diffusion generated by the advection schemes). Implicit numerical diffusion can provide a large contribution to the total mixing, especially at coarse grid resolution (such as those used in our simulations), and can cause numerical entrainment (Yamaguchi et al., 2011). Therefore it is possible that the SAM model at coarse resolutions is characterized by a large numerical diffusion which represents a substantial part of the total mixing of the model. As a matter of fact, the SAM solution is found to be substantially unaltered by switching off the explicit turbulence model. This approach resembles the one used in Implicit Large Eddy Simulations (ILES). In contrast, in the WRF model, which is built with higher-order numerics for running at coarse resolution, most part of the mixing is provided by the turbulent subgrid-scale parametrization. Accordingly, a substantial change of the WRF solution is observed by switching off the turbulence model.

We have shown that reducing the numerical and turbulent diffusion in SAMh (by refining horizontal resolution) is sufficient to prevent the onset of CSA. A finer resolution and lower diffusion is found to decrease also the amount of shallow clouds in driest regions and this may be interpreted as the main cause behind the absence of CSA at finer resolutions (C. J. Muller & Held, 2012). However, the reintroduction of a large explicit mixing in SAM3h, allows the onset of CSA at finer resolution, even with a small amount of shallow clouds. Therefore shallow clouds and their effect on radiative cooling, do not seem to play a significant role in the triggering of CSA. Instead they may be considered fundamental at later stages for its development and intensification. It is not trivial to find out which part of SAM numerics is providing the largest contribution to

numerical diffusion when using such model at coarse resolution. This may be the large integration time step in the AB3 scheme, the SOC momentum advection scheme, or the scalar advection scheme (although this work adopted the highest-order available Yamaguchi et al. (2011)).

The key ingredient common to all numerical simulations showing the onset of CSA is the initial large-scale horizontal variability of convection. This is examined by looking at the horizontal energy spectra of Total Water Path. It is shown that a larger horizontal variability at large-scales is necessary to introduce large dry perturbations in the free troposphere and to cause the initial free-tropospheric drying. Such an initial large-scale variability is found since the first days of the simulation. Therefore it cannot be created trough a slow process such as the radiative subsidence, as calculated by the Weak Temperature Gradient hypothesis, but must be traced back to a fast and efficient process linked to the environment for convection, such as lateral mixing. An efficient lateral mixing will dilute updraft in dry regions, reducing the convectively-induced moistening of the free-troposphere and enhancing the large-scale variability of convection. Once such pre-condition of free tropospheric drying is verified, then a strong deep circulation between moist and dry regions can develop, intruding dry air into the boundary layer and creating a high surface pressure anomaly which is recognized to be fundamental for the development of CSA (B. Yang & Tan, 2020; Shamekh et al., 2020).

The necessity of an initial large scale variability in moisture and convection to trigger CSA was hypothesized by Windmiller and Craig (2019) and it is consistent with recent results by Yanase et al. (2022) and Biagioli and Tompkins (2023). In particular, Yanase et al. (2022) demonstrated with the SCALE model that the radiative mechanism is not caused directly by the WTG velocity, but by the indirect path trough the environment for convection. Biagioli and Tompkins (2023) offer a reinterpretation of results by Tompkins and Semie (2017) attributing the sensitivity of CSA to diffusion to the mean upraft size instead of the effect of humidity entrainment into updrafts. Here we add a further step, by demonstrating that in CRM models, the initial large-scale variability of convection (free-tropospheric dry perturbation and mean updraft size) is set by small-scale mixing processes. The importance of energy dissipation in convective permitting models at coarse resolution was also found to be critical for shallow convective self-aggregation by Janssens et al. (2022). Interestingly, the appearence of larger and more energetic structures by damping small-scale structures (imposing larger values of the Smagorinsky constant) is also a common feature in Large Eddy Simulations of turbulent channel flows (Hwang & Cossu, 2010).

In this paper the moisture-convection feedback was found to be fundamental for the triggering of CSA. Our results appear to contrast with those of D. Yang (2019), who show that CSA can be observed even by removing the MC feedback (homogenizing the water vapor field each 3 hours). However D. Yang (2019) uses the SAM model at 2 km horizontal resolution, which we have shown to be strongly affected by numerical mixing processes. Moreover, the homogenization time scale (3 hours) of the water vapor could be too large to effectively turn off the moisture-convection feedback, as also estimated by Ramirez Reyes (2023). Therefore the final aggregated state obtained by D. Yang (2019), which exhibit a very small variance of precipitable water with respect to what is usually observed in CSA studies, could be model dependent. Further work is needed to replicate the experiments of D. Yang (2019) in other CRMs.

This pre-condition on initial large-scale variability of convection for the triggering of CSA, can also explain three different properties that characterize self-aggregation in numerical simulations: 1) the sensitivity to horizontal grid resolution; 2) the sensitivity to domain size, 3) the hysteresis of self-aggregation. The finer the resolution, the smaller the numerical and explicit entrainment, the smaller the updraft dilution, the smaller the large-scale variability and the smaller the free tropospheric drying. Therefore at finer resolutions, unless we do not keep fixed the mean updraft size and entrainment, CSA will not occur. At the same time, the larger the domain size, the larger the maximum allowed horizontal variability of water vapor and the larger the possibility to trigger CSA. These

two arguments can explain why the regime diagram of CSA (the sensitivity of CSA to horizontal resolution and domain size) is different in different models. Using the SCALE model, Yanase et al. (2020) found CSA to occur even at 500 m, while for the SAM model no self-aggregation was found below 2 km (C. J. Muller & Held, 2012). Regarding the hysteresis of self-aggregation, starting the simulation from an already aggregated condition, sets the initial large-scale variability to a fixed large value and we expect no sensitivity to horizontal resolution (C. J. Muller & Held, 2012) or turbulent mixing (Tompkins & Semie, 2017).

Many studies investigate the role of other important factors other than subgrid-scale mixing in the triggering of CSA, such as vertical resolution (Jenney et al., 2023), grid anisotropy (De Roode et al., 2022), microphysics (Shi & Fan, 2021), rotation (Carstens & Wing, 2022) and SST (Wing & Emanuel, 2014; Coppin & Bony, 2015; M. Khairoutdinov & Emanuel, 2013). Future work is needed to investigate whether the hypothesized pre-condition on large-scale horizontal variability in convection for trigger of CSA would be valid for different values of the above cited factors.

6 Conclusions

The representation of mixing at small scales remains a substantial problem for many large-scale geophysical flows (Mapes & Neale, 2011). In particular, mixing processes affect the amount of cloud condensate (Jeevanjee & Zhou, 2022), the free-tropospheric relative humidity in the tropics (Grabowski & Moncrieff, 2004), and the organization of convection (Takemi & Rotunno, 2003; Tompkins & Semie, 2017). Therefore small-scale mixing processes may have important implications for climate.

This work focuses on convective self-aggregation, which spontaneously occurs in idealized simulations of Radiative-Convective Equilibrium. It is shown that this phenomenon exhibits a strong sensitivity to mixing and entrainment processes, as represented by both the explicit turbulence model and the numerical dissipation. In particular mixing is responsible for setting the initial large-scale variability of free tropospheric moisture and therefore allowing the development of different radiative cooling rates between dry and moist regions. When refining horizontal grid resolution and decreasing numerical dissipation, enough turbulent mixing is necessary for the spontaneous development of convective aggregation. In such condition, convective self-aggregation is found to develop also with relatively small amount of shallow clouds. Therefore, turbulent mixing and dissipation at small scales regulate the amplitude of humidity perturbations introduced by convection in the free troposphere: the larger the dissipation at small scales, the larger the size and the strength of humidity perturbations in the free troposphere, which can destabilize the RCE state. A large initial horizontal variability of convection is found to be necessary for drying the free troposphere and trigger the occurrence of CSA.

Until horizontal grid resolution down to the inertial range for deep convection is achieved (100 m, Bryan et al., 2003), non-homogeneous entrainment processes will not be resolved and the response of deep convection to moisture perturbation will be tightly linked to the numerics and the SGS turbulence parametrization adopted by the models. Less idealized Global Cloud Resolving Models (GCRM) should take into account such dependence of mesoscale organization both on numerical and SGS mixing. TWP energy spectra have been shown to be a useful diagnostic tool for assessing the initial large scale variability of convection and its influence on mesoscale organization. In particular, such large-scale variability should not vary with the coarsening/refinement of horizontal resolution and should be comparable to observations. A correct representation of large-scale horizontal variability of convection will also affect the reproduction of MJO events, as demonstrated by Holloway et al. (2013).

In pursuit of these results, new families of turbulence models should be adopted for anisotropic and coarse resolution grids (Honnert et al., 2021; Cimarelli et al., 2019) and the idealized RCE simulations could provide a useful setting for studying their impact on deep convection.

7 Open Research

All data and post-processing python scripts necessary for reproducing the results of the paper are available at `https://doi.org/10.5281/zenodo.7799005`. SAM and WRF codes are available at `http://rossby.msrc.sunysb.edu/~marat/SAM/` and `https://github.com/wrf-model/WRF`, respectively.

Acknowledgments

This research has been funded by the Italian Ministry of University and Research (MIUR) and the University of Perugia by the *Fondo Ricerca di Ateneo esercizio 2021: Cambiamenti climatici: consapevolezza impatto sociale, modelli scientifici e soluzioni tecnologiche*. The authors thank Andrea Cimarelli for the useful discussion during the development of this work. Lastly, the authors want to acknowledge high performance computing support from ECMWF Supercomputing facilities and the Italian Air Force, which allowed us extensive use of the HPC facilities of the CRAY XC40 to compute the high resolution simulations included in this paper.

References

Biagioli, G., & Tompkins, A. M. (2023). A dimensionless parameter for predicting convective self-aggregation onset in a stochastic reaction-diffusion model of tropical radiative-convective equilibrium. *Journal of Advances in Modeling Earth Systems*, *15*(5), e2022MS003231.

Bony, S., Stevens, B., Coppin, D., Becker, T., Reed, K. A., Voigt, A., & Medeiros, B. (2016). Thermodynamic control of anvil cloud amount. *Proceedings of the National Academy of Sciences*, *113*(32), 8927–8932.

Bretherton, C., & Blossey, P. (2017). Understanding mesoscale aggregation of shallow cumulus convection using large-eddy simulation. *Journal of Advances in Modeling Earth Systems*, *9*(8), 2798–2821.

Bretherton, C. S., Blossey, P. N., & Khairoutdinov, M. (2005). An energy-balance analysis of deep convective self-aggregation above uniform sst. *Journal of the atmospheric sciences*, *62*(12), 4273–4292.

Bryan, G. H. (2005). Spurious convective organization in simulated squall lines owing to moist absolutely unstable layers. *Monthly weather review*, *133*(7), 1978–1997.

Bryan, G. H., Wyngaard, J. C., & Fritsch, J. M. (2003). Resolution requirements for the simulation of deep moist convection. *Monthly Weather Review*, *131*(10), 2394–2416.

Carstens, J. D., & Wing, A. A. (2022). A spectrum of convective self-aggregation based on background rotation. *Journal of Advances in Modeling Earth Systems*, *14*(5), e2021MS002860.

Cerlini, P. B., Saraceni, M., & Silvestri, L. (2023). Competing effect of radiative and moisture feedback in convective aggregation states in two crms. *Journal of Advances in Modeling Earth Systems*, *15*(2), e2022MS003323.

Chen, S.-H., & Sun, W.-Y. (2002). A one-dimensional time dependent cloud model. *Journal of the Meteorological Society of Japan. Ser. II*, *80*(1), 99–118.

Cimarelli, A., Abbà, A., & Germano, M. (2019). General formalism for a reduced description and modelling of momentum and energy transfer in turbulence. *Journal of Fluid Mechanics*, *866*, 865–896.

Colin, M., Sherwood, S., Geoffroy, O., Bony, S., & Fuchs, D. (2019). Identifying the sources of convective memory in cloud-resolving simulations. *Journal of the Atmospheric Sciences*, *76*(3), 947–962.

Collins, W. D., Rasch, P. J., Boville, B. A., Hack, J. J., McCaa, J. R., Williamson, D. L., ... Zhang, M. (2006). The formulation and atmospheric simulation

of the community atmosphere model version 3 (cam3). *Journal of Climate*, *19*(11), 2144–2161.

Coppin, D., & Bony, S. (2015). Physical mechanisms controlling the initiation of convective self-aggregation in a general circulation model. *Journal of Advances in Modeling Earth Systems*, *7*(4), 2060–2078.

Craig, G. C., & Mack, J. M. (2013). A coarsening model for self-organization of tropical convection. *Journal of Geophysical Research: Atmospheres*, *118*(16), 8761–8769.

Deardorff, J. W. (1980). Stratocumulus-capped mixed layers derived from a three-dimensional model. *Boundary-layer meteorology*, *18*(4), 495–527.

De Roode, S. R., Siebesma, A. P., Jansson, F., & Janssens, M. (2022). Dependency of mesoscale organization on grid anisotropy in large-eddy simulations of convective boundary layers at gray zone resolutions. *Journal of Advances in Modeling Earth Systems*, *14*(11), e2022MS003095.

Durran, D., Weyn, J. A., & Menchaca, M. Q. (2017). Practical considerations for computing dimensional spectra from gridded data. *Monthly Weather Review*, *145*(9), 3901–3910.

Durran, D. R. (2010). *Numerical methods for fluid dynamics: With applications to geophysics* (Vol. 32). Springer Science & Business Media.

Durran, D. R., & Klemp, J. B. (1982). On the effects of moisture on the brunt-väisälä frequency. *Journal of Atmospheric Sciences*, *39*(10), 2152–2158.

Emanuel, K., Wing, A. A., & Vincent, E. M. (2014). Radiative-convective instability. *Journal of Advances in Modeling Earth Systems*, *6*(1), 75–90.

Grabowski, W. W., & Moncrieff, M. (2004). Moisture–convection feedback in the tropics. *Quarterly Journal of the Royal Meteorological Society: A journal of the atmospheric sciences, applied meteorology and physical oceanography*, *130*(604), 3081–3104.

Grant, L. D., & van den Heever, S. C. (2016). Cold pool dissipation. *Journal of Geophysical Research: Atmospheres*, *121*(3), 1138–1155.

Held, I. M., Hemler, R. S., & Ramaswamy, V. (1993). Radiative-convective equilibrium with explicit two-dimensional moist convection. *Journal of Atmospheric Sciences*, *50*(23), 3909–3927.

Hohenegger, C., & Stevens, B. (2016). Coupled radiative convective equilibrium simulations with explicit and parameterized convection. *Journal of Advances in Modeling Earth Systems*, *8*(3), 1468–1482.

Holloway, C. E., & Woolnough, S. J. (2016). The sensitivity of convective aggregation to diabatic processes in idealized radiative-convective equilibrium simulations. *Journal of Advances in Modeling Earth Systems*, *8*(1), 166–195.

Holloway, C. E., Woolnough, S. J., & Lister, G. M. (2013). The effects of explicit versus parameterized convection on the mjo in a large-domain high-resolution tropical case study. part i: Characterization of large-scale organization and propagation. *Journal of the Atmospheric Sciences*, *70*(5), 1342–1369.

Hong, S.-Y., Noh, Y., & Dudhia, J. (2006). A new vertical diffusion package with an explicit treatment of entrainment processes. *Monthly weather review*, *134*(9), 2318–2341.

Honnert, R., Masson, V., Lac, C., & Nagel, T. (2021). A theoretical analysis of mixing length for atmospheric models from micro to large scales. *Frontiers in Earth Science*, *8*, 582056.

Hwang, Y., & Cossu, C. (2010). Self-sustained process at large scales in turbulent channel flow. *Physical review letters*, *105*(4), 044505.

Iacono, M. J., Delamere, J. S., Mlawer, E. J., Shephard, M. W., Clough, S. A., & Collins, W. D. (2008). Radiative forcing by long-lived greenhouse gases: Calculations with the aer radiative transfer models. *Journal of Geophysical Research: Atmospheres*, *113*(D13).

Jablonowski, C., & Williamson, D. L. (2011). The pros and cons of diffusion, fil-

ters and fixers in atmospheric general circulation models. In P. Lauritzen, C. Jablonowski, M. Taylor, & R. Nair (Eds.), *Numerical techniques for global atmospheric models* (pp. 381–493). Berlin, Heidelberg: Springer Berlin Heidelberg. Retrieved from https://doi.org/10.1007/978-3-642-11640-7_13 doi: 10.1007/978-3-642-11640-7_13

Jakob, C., Singh, M., & Jungandreas, L. (2019). Radiative convective equilibrium and organized convection: An observational perspective. *Journal of Geophysical Research: Atmospheres*, *124*(10), 5418–5430.

Janssens, M., Vilà-Guerau de Arellano, J., Van Heerwaarden, C. C., Van Stratum, B. J., De Roode, S. R., Siebesma, A. P., & Glassmeier, F. (2022). The time scale of shallow convective self-aggregation in large-eddy simulations is sensitive to numerics. *Journal of Advances in Modeling Earth Systems*, e2022MS003292.

Jeevanjee, N., & Romps, D. M. (2013). Convective self-aggregation, cold pools, and domain size. *Geophysical Research Letters*, *40*(5), 994–998.

Jeevanjee, N., & Zhou, L. (2022). On the resolution-dependence of anvil cloud fraction and precipitation efficiency in radiative-convective equilibrium. *Journal of Advances in Modeling Earth Systems*, *14*(3), e2021MS002759.

Jenney, A. M., Ferretti, S. L., & Pritchard, M. S. (2023). Vertical resolution impacts explicit simulation of deep convection. *Journal of Advances in Modeling Earth Systems*, *15*(10), e2022MS003444.

Jiménez, P. A., & Dudhia, J. (2012). Improving the representation of resolved and unresolved topographic effects on surface wind in the wrf model. *Journal of Applied Meteorology and Climatology*, *51*(2), 300–316.

Khairoutdinov, M., & Emanuel, K. (2013). Rotating radiative-convective equilibrium simulated by a cloud-resolving model. *Journal of Advances in Modeling Earth Systems*, *5*(4), 816–825.

Khairoutdinov, M. F., & Randall, D. A. (2003). Cloud resolving modeling of the arm summer 1997 iop: Model formulation, results, uncertainties, and sensitivities. *Journal of Atmospheric Sciences*, *60*(4), 607–625.

Knievel, J. C., Bryan, G. H., & Hacker, J. P. (2007). Explicit numerical diffusion in the wrf model. *Monthly Weather Review*, *135*(11), 3808–3824.

Kurowski, M. J., Grabowski, W. W., & Smolarkiewicz, P. K. (2014). Anelastic and compressible simulation of moist deep convection. *Journal of the Atmospheric Sciences*, *71*(10), 3767–3787.

Lai, K. T., & Waite, M. L. (2023). Kinetic energy spectra and spectral budget of radiative-convective equilibrium. *Journal of the Atmospheric Sciences*.

Lilly, D. K. (1962). On the numerical simulation of buoyant convection. *Tellus*, *14*(2), 148–172.

Lindborg, E. (1999). Can the atmospheric kinetic energy spectrum be explained by two-dimensional turbulence? *Journal of Fluid Mechanics*, *388*, 259–288.

Mapes, B., & Neale, R. (2011). Parameterizing convective organization to escape the entrainment dilemma. *Journal of Advances in Modeling Earth Systems*, *3*(2).

Muller, C., & Bony, S. (2015). What favors convective aggregation and why? *Geophysical Research Letters*, *42*(13), 5626–5634.

Muller, C., Yang, D., Craig, G., Cronin, T., Fildier, B., Haerter, J. O., ... others (2022). Spontaneous aggregation of convective storms. *Annual Review of Fluid Mechanics*, *54*, 133–157.

Muller, C. J., & Held, I. M. (2012). Detailed investigation of the self-aggregation of convection in cloud-resolving simulations. *Journal of the Atmospheric Sciences*, *69*(8), 2551–2565.

Nastrom, G. D., & Gage, K. S. (1985). A climatology of atmospheric wavenumber spectra of wind and temperature observed by commercial aircraft. *Journal of Atmospheric Sciences*, *42*(9), 950 - 960. Retrieved from https://journals.ametsoc.org/view/journals/atsc/42/9/1520-0469

_1985_042_0950_acoaws_2_0_co_2.xml doi: https://doi.org/10.1175/1520-0469(1985)042⟨0950:ACOAWS⟩2.0.CO;2

Nishizawa, S., Yashiro, H., Sato, Y., Miyamoto, Y., & Tomita, H. (2015). Influence of grid aspect ratio on planetary boundary layer turbulence in large-eddy simulations. *Geoscientific Model Development*, *8*(10), 3393–3419.

Noh, Y., Cheon, W., Hong, S., & Raasch, S. (2003). Improvement of the k-profile model for the planetary boundary layer based on large eddy simulation data. *Boundary-layer meteorology*, *107*(2), 401–427.

Nolan, D. S., Rappin, E. D., & Emanuel, K. A. (2007). Tropical cyclogenesis sensitivity to environmental parameters in radiative–convective equilibrium. *Quarterly Journal of the Royal Meteorological Society: A journal of the atmospheric sciences, applied meteorology and physical oceanography*, *133*(629), 2085–2107.

Patrizio, C. R., & Randall, D. A. (2019). Sensitivity of convective self-aggregation to domain size. *Journal of Advances in Modeling Earth Systems*, *11*(7), 1995–2019.

Pressel, K. G., Mishra, S., Schneider, T., Kaul, C. M., & Tan, Z. (2017). Numerics and subgrid-scale modeling in large eddy simulations of stratocumulus clouds. *Journal of advances in modeling earth systems*, *9*(2), 1342–1365.

Ramirez Reyes, A. (2023). *Looking for the minimal recipe for spontaneous tc genesis* (Unpublished doctoral dissertation). UC Davis.

Ramírez Reyes, A., & Yang, D. (2021). Spontaneous cyclogenesis without radiative and surface-flux feedbacks. *Journal of the Atmospheric Sciences*, *78*(12), 4169–4184.

Rappin, E. D., Nolan, D. S., & Emanuel, K. A. (2010). Thermodynamic control of tropical cyclogenesis in environments of radiative-convective equilibrium with shear. *Quarterly Journal of the Royal Meteorological Society*, *136*(653), 1954–1971.

Shamekh, S., Muller, C., Duvel, J.-P., & d'Andrea, F. (2020). Self-aggregation of convective clouds with interactive sea surface temperature. *Journal of Advances in Modeling Earth Systems*, *12*(11), e2020MS002164.

Shi, X., & Fan, Y. (2021). Modulation of the bifurcation in radiative-convective equilibrium by gray-zone cloud and turbulence parameterizations. *Journal of Advances in Modeling Earth Systems*, *13*(10), e2021MS002632.

Simon, J. S., & Chow, F. K. (2021). Alternative anisotropic formulations for eddy-viscosity models in the weather research and forecasting model. *Boundary-Layer Meteorology*, *181*(1), 11–37.

Singh, M. S., & O'Gorman, P. A. (2013). Influence of entrainment on the thermal stratification in simulations of radiative-convective equilibrium. *Geophysical Research Letters*, *40*(16), 4398–4403.

Skamarock, W. C. (2004). Evaluating mesoscale nwp models using kinetic energy spectra. *Monthly weather review*, *132*(12), 3019–3032.

Skamarock, W. C., Klemp, J. B., Dudhia, J., Gill, D. O., Liu, Z., Berner, J., ... others (2019). A description of the advanced research wrf model version 4. *National Center for Atmospheric Research: Boulder, CO, USA*, *145*, 145.

Skamarock, W. C., & Weisman, M. L. (2009). The impact of positive-definite moisture transport on nwp precipitation forecasts. *Monthly Weather Review*, *137*(1), 488–494.

Smagorinsky, J. (1963). General circulation experiments with the primitive equations: I. the basic experiment. *Monthly weather review*, *91*(3), 99–164.

Smolarkiewicz, P. K., & Grabowski, W. W. (1990). The multidimensional positive definite advection transport algorithm: Nonoscillatory option. *Journal of Computational Physics*, *86*(2), 355–375.

Stauffer, C. L., & Wing, A. A. (2022). Properties, changes, and controls of deep-convecting clouds in radiative-convective equilibrium. *Journal of Advances in Modeling Earth Systems*, *14*(6), e2021MS002917.

Takemi, T., & Rotunno, R. (2003). The effects of subgrid model mixing and numerical filtering in simulations of mesoscale cloud systems. *Monthly Weather Review*, *131*(9), 2085–2101.

Tompkins, A. M. (2001). Organization of tropical convection in low vertical wind shears: The role of water vapor. *Journal of the atmospheric sciences*, *58*(6), 529–545.

Tompkins, A. M., & Craig, G. C. (1998). Radiative–convective equilibrium in a three-dimensional cloud-ensemble model. *Quarterly Journal of the Royal Meteorological Society*, *124*(550), 2073–2097.

Tompkins, A. M., & Semie, A. G. (2017). Organization of tropical convection in low vertical wind shears: Role of updraft entrainment. *Journal of Advances in Modeling Earth Systems*, *9*(2), 1046–1068.

Wang, H., Skamarock, W. C., & Feingold, G. (2009). Evaluation of scalar advection schemes in the advanced research wrf model using large-eddy simulations of aerosol–cloud interactions. *Monthly Weather Review*, *137*(8), 2547–2558.

Wicker, L. J., & Skamarock, W. C. (2002). Time-splitting methods for elastic models using forward time schemes. *Monthly weather review*, *130*(8), 2088–2097.

Windmiller, J. M., & Craig, G. C. (2019). Universality in the spatial evolution of self-aggregation of tropical convection. *Journal of the Atmospheric Sciences*, *76*(6), 1677–1696.

Wing, A. A., Camargo, S. J., & Sobel, A. H. (2016). Role of radiative–convective feedbacks in spontaneous tropical cyclogenesis in idealized numerical simulations. *Journal of the Atmospheric Sciences*, *73*(7), 2633–2642.

Wing, A. A., Emanuel, K., Holloway, C. E., & Muller, C. (2017). Convective self-aggregation in numerical simulations: A review. *Shallow clouds, water vapor, circulation, and climate sensitivity*, 1–25.

Wing, A. A., & Emanuel, K. A. (2014). Physical mechanisms controlling self-aggregation of convection in idealized numerical modeling simulations. *Journal of Advances in Modeling Earth Systems*, *6*(1), 59–74.

Wing, A. A., Stauffer, C. L., Becker, T., Reed, K. A., Ahn, M.-S., Arnold, N. P., ... others (2020). Clouds and convective self-aggregation in a multimodel ensemble of radiative-convective equilibrium simulations. *Journal of advances in modeling earth systems*, *12*(9), e2020MS002138.

Xue, M. (2000). High-order monotonic numerical diffusion and smoothing. *Monthly Weather Review*, *128*(8), 2853–2864.

Yamaguchi, T., Randall, D. A., & Khairoutdinov, M. F. (2011). Cloud modeling tests of the ultimate–macho scalar advection scheme. *Monthly Weather Review*, *139*(10), 3248–3264.

Yanase, T., Nishizawa, S., Miura, H., Takemi, T., & Tomita, H. (2020). New critical length for the onset of self-aggregation of moist convection. *Geophysical Research Letters*, *47*(16), e2020GL088763.

Yanase, T., Nishizawa, S., Miura, H., Takemi, T., & Tomita, H. (2022). Low-level circulation and its coupling with free-tropospheric variability as a mechanism of spontaneous aggregation of moist convection. *Journal of the Atmospheric Sciences*, *79*(12), 3429–3451.

Yang, B., & Tan, Z.-M. (2020). The initiation of dry patches in cloud-resolving convective self-aggregation simulations: Boundary layer dry-subsidence feedback. *Journal of the Atmospheric Sciences*, *77*(12), 4129–4141.

Yang, D. (2018). Boundary layer height and buoyancy determine the horizontal scale of convective self-aggregation. *Journal of the Atmospheric Sciences*, *75*(2), 469–478.

Yang, D. (2019). Convective heating leads to self-aggregation by generating available potential energy. *Geophysical Research Letters*, *46*(17-18), 10687–10696.

Figure 1.

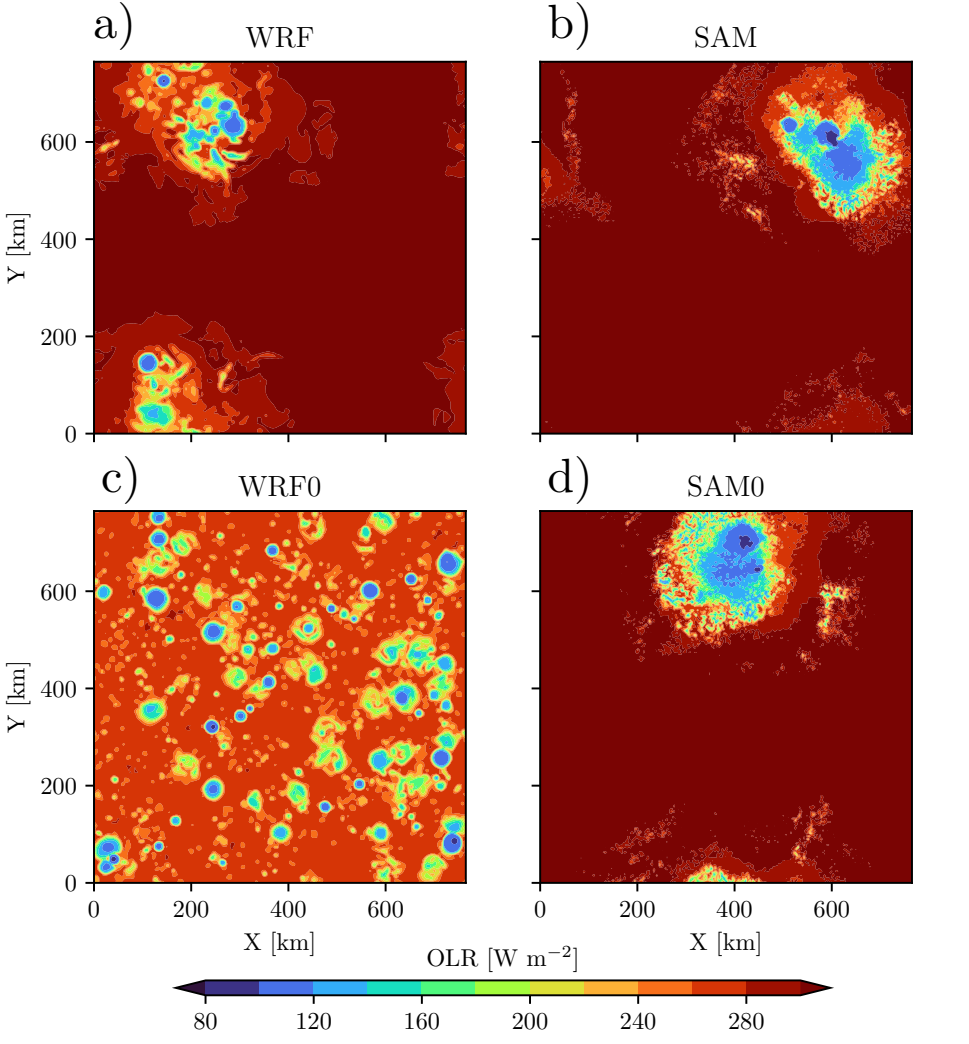
a)
WRF
b)
SAM
c)
WRF0
d)
SAM0
Y [km]
X [km]
0
200
400
600
OLR [W m^{-2}]
80
120
160
200
240
280

Figure 2.

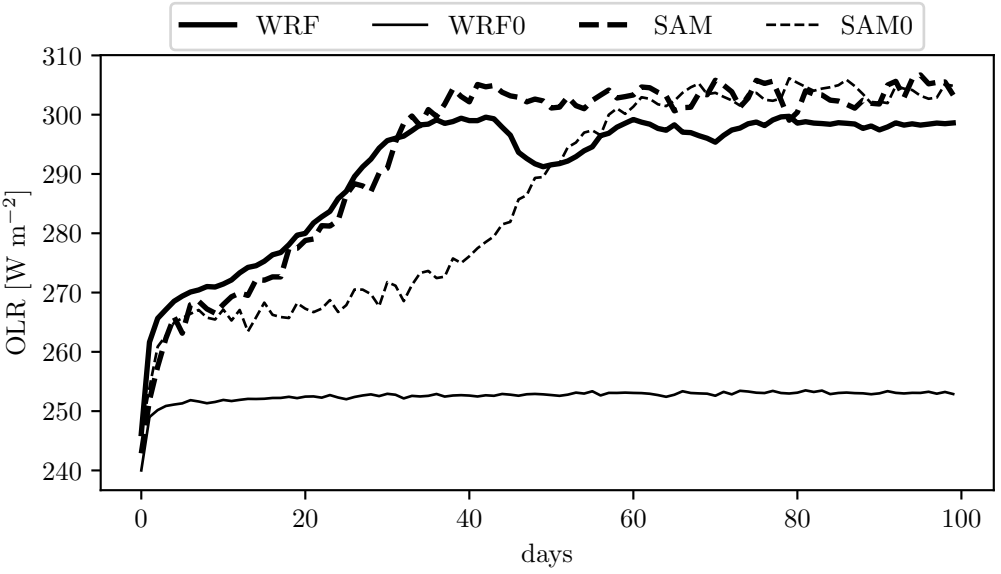
WRF
WRF0
SAM
SAM0
310
300
290
280
270
260
250
240
OLR [W m^{-2}]
0
20
40
60
80
100
days

Figure 3.

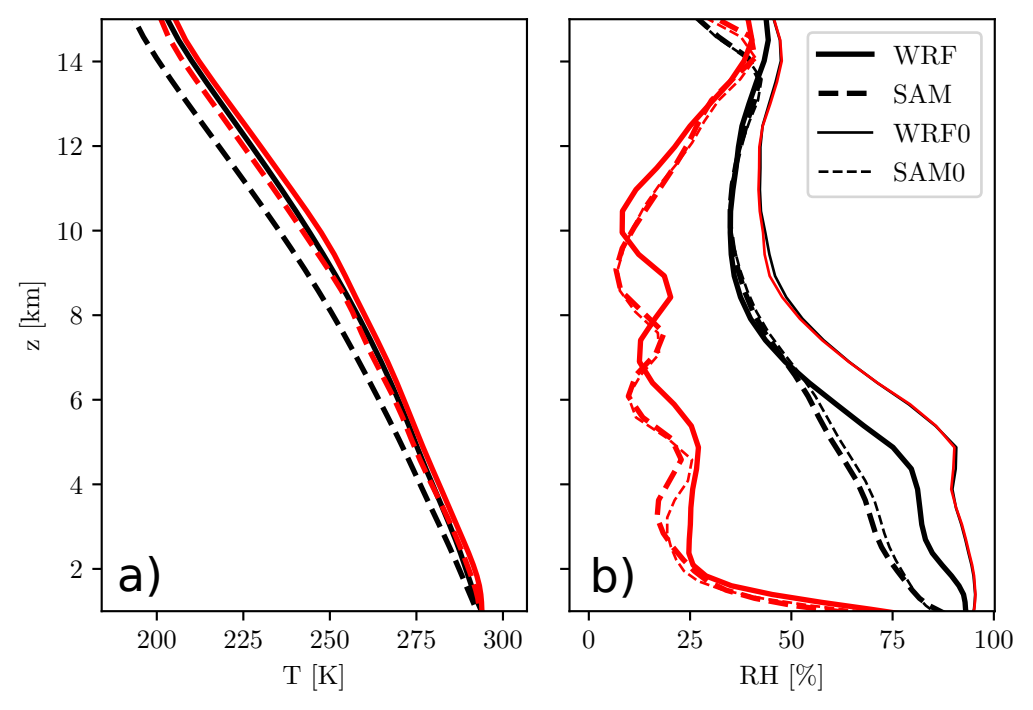
z [km]
14
12
10
8
6
4
2
a)
200
225
250
275
300
T [K]
b)
0
25
50
75
100
RH [%]
WRF
SAM
WRF0
SAM0

Figure 4.

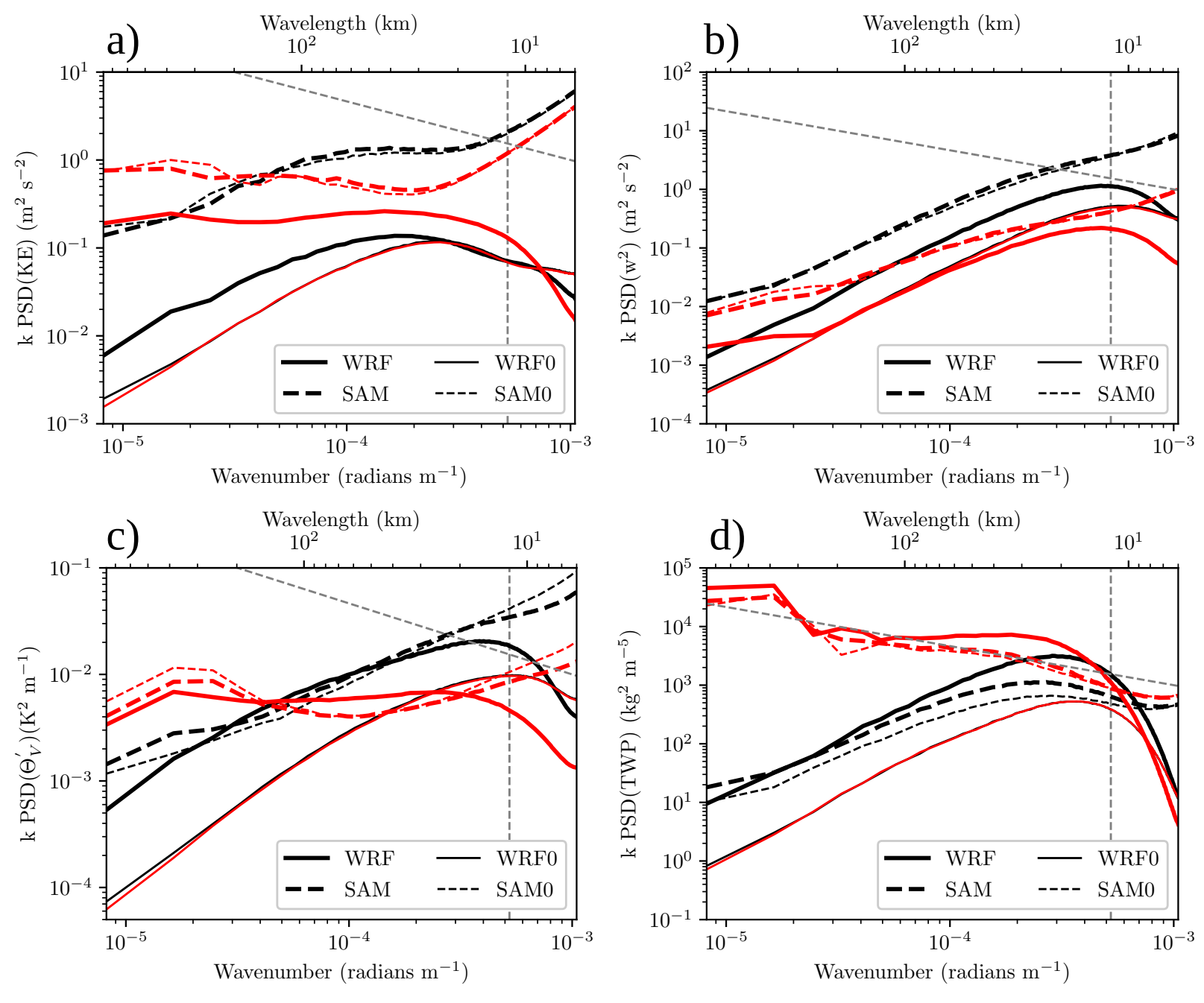
a)
Wavelength (km)
10^2
10^1
10^1
10^0
10^{-1}
10^{-2}
10^{-3}
k PSD(KE) (m^2 s^{-2})
WRF
WRF0
SAM
SAM0
10^{-5}
10^{-4}
10^{-3}
Wavenumber (radians m^{-1})
b)
Wavelength (km)
10^2
10^1
10^2
10^1
10^0
10^{-1}
10^{-2}
10^{-3}
10^{-4}
k PSD(w^2) (m^2 s^{-2})
WRF
WRF0
SAM
SAM0
10^{-5}
10^{-4}
10^{-3}
Wavenumber (radians m^{-1})
c)
Wavelength (km)
10^2
10^1
10^{-1}
10^{-2}
10^{-3}
10^{-4}
k PSD(Θ_V')(K^2 m^{-1})
WRF
WRF0
SAM
SAM0
10^{-5}
10^{-4}
10^{-3}
Wavenumber (radians m^{-1})
d)
Wavelength (km)
10^2
10^1
10^5
10^4
10^3
10^2
10^1
10^0
10^{-1}
k PSD(TWP) (kg^2 m^{-5})
WRF
WRF0
SAM
SAM0
10^{-5}
10^{-4}
10^{-3}
Wavenumber (radians m^{-1})

Figure 5.

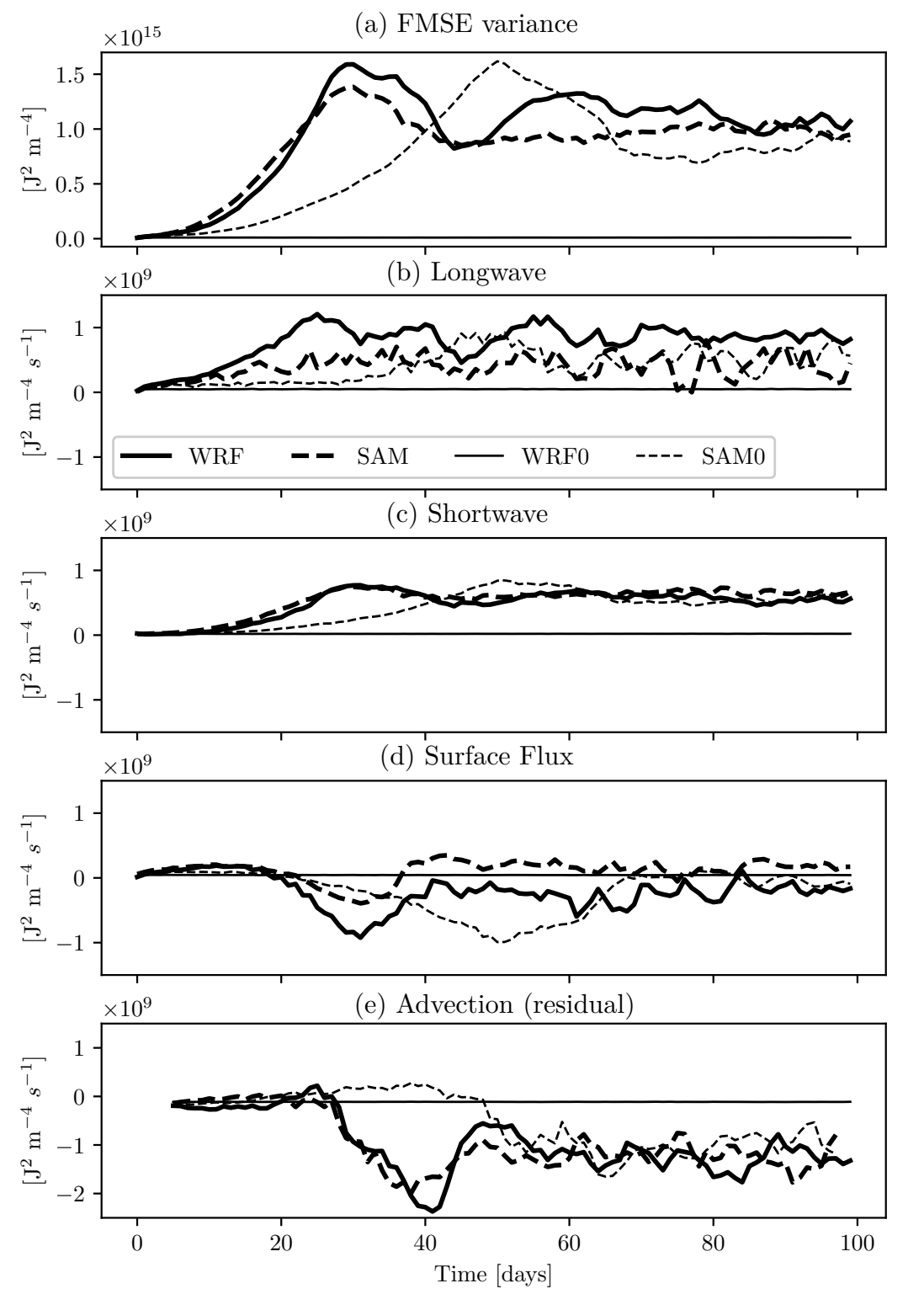
(a) FMSE variance
$\times 10^{15}$
$[J^2\ m^{-4}]$
1.5
1.0
0.5
0.0
(b) Longwave
$\times 10^{9}$
$[J^2\ m^{-4}\ s^{-1}]$
1
0
−1
WRF
SAM
WRF0
SAM0
(c) Shortwave
$\times 10^{9}$
$[J^2\ m^{-4}\ s^{-1}]$
1
0
−1
(d) Surface Flux
$\times 10^{9}$
$[J^2\ m^{-4}\ s^{-1}]$
1
0
−1
(e) Advection (residual)
$\times 10^{9}$
$[J^2\ m^{-4}\ s^{-1}]$
1
0
−1
−2
0
20
40
60
80
100
Time [days]

Figure 6.

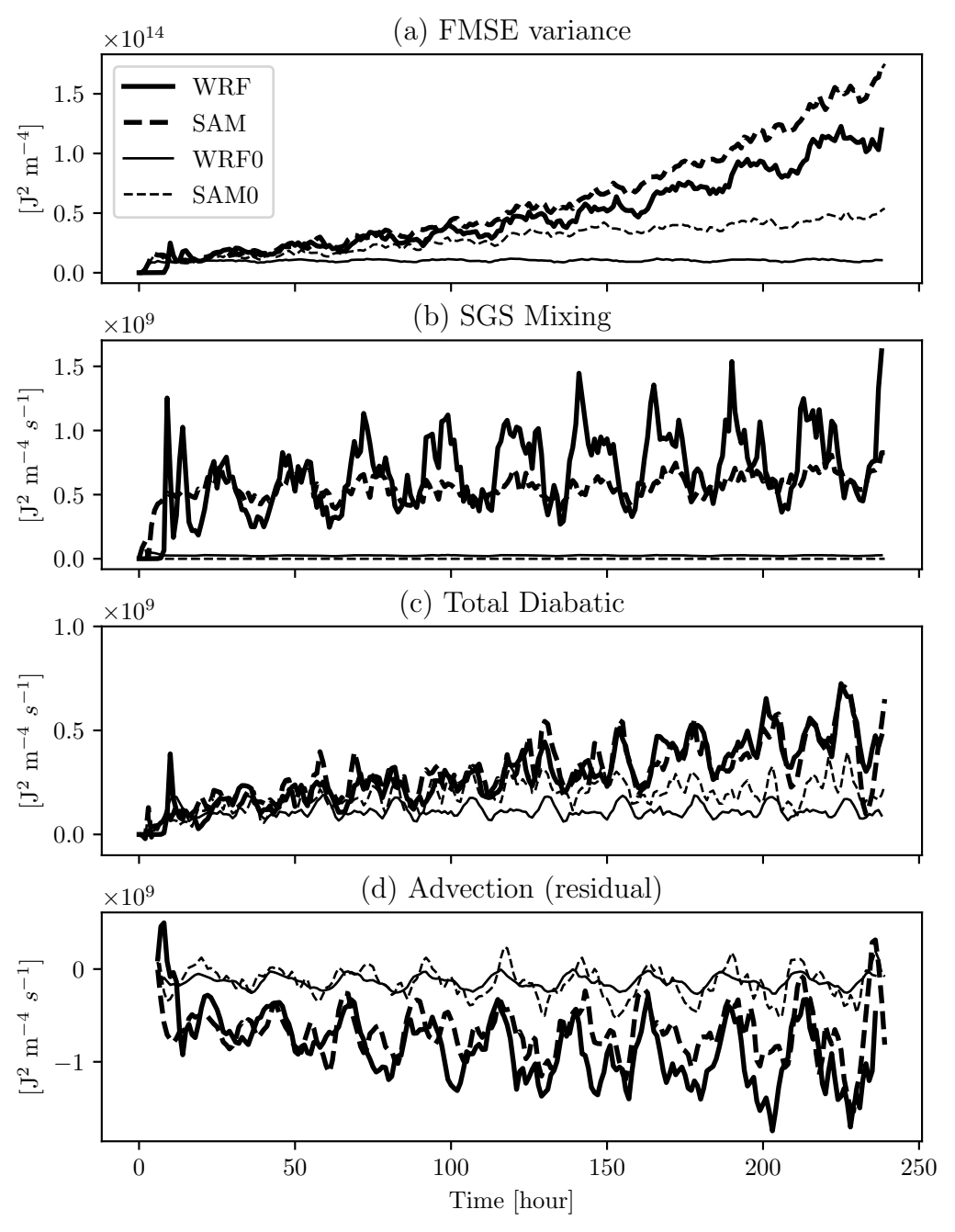
(a) FMSE variance
×10^14
WRF
SAM
WRF0
SAM0
[J^2 m^-4]
(b) SGS Mixing
×10^9
[J^2 m^-4 s^-1]
(c) Total Diabatic
×10^9
[J^2 m^-4 s^-1]
(d) Advection (residual)
×10^9
[J^2 m^-4 s^-1]
Time [hour]

Figure 7.

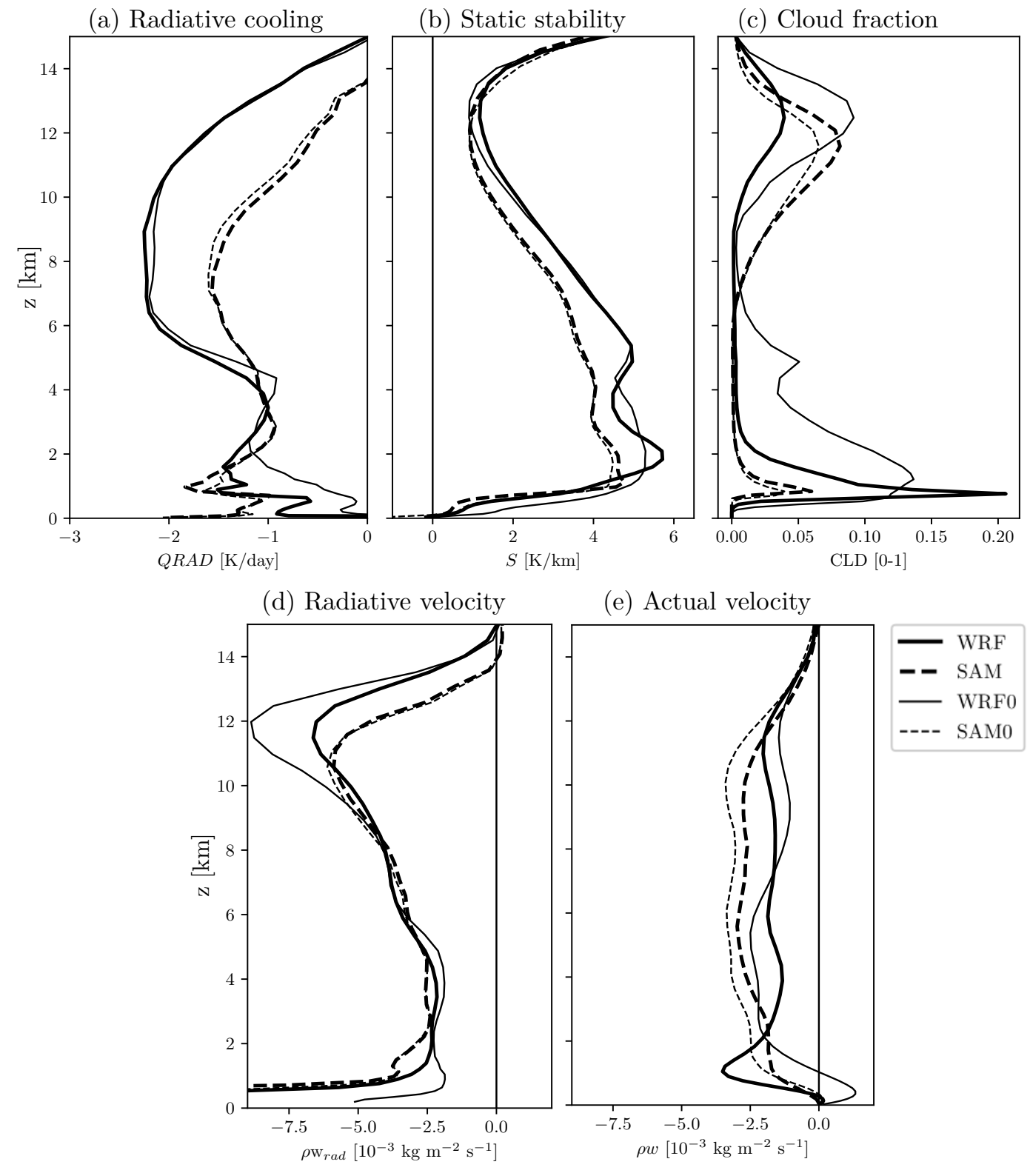
(a) Radiative cooling
(b) Static stability
(c) Cloud fraction
(d) Radiative velocity
(e) Actual velocity
z [km]
$QRAD$ [K/day]
S [K/km]
CLD [0-1]
ρw_{rad} [10^{-3} kg m^{-2} s^{-1}]
ρw [10^{-3} kg m^{-2} s^{-1}]
WRF
SAM
WRF0
SAM0

Figure 8.

(a) WRFs

(b) WRF0s

Y [km]

600

400

200

0

0

200

400

600

X [km]

X [km]

OLR [W m^{-2}]

80

120

160

200

240

280

Figure 9.

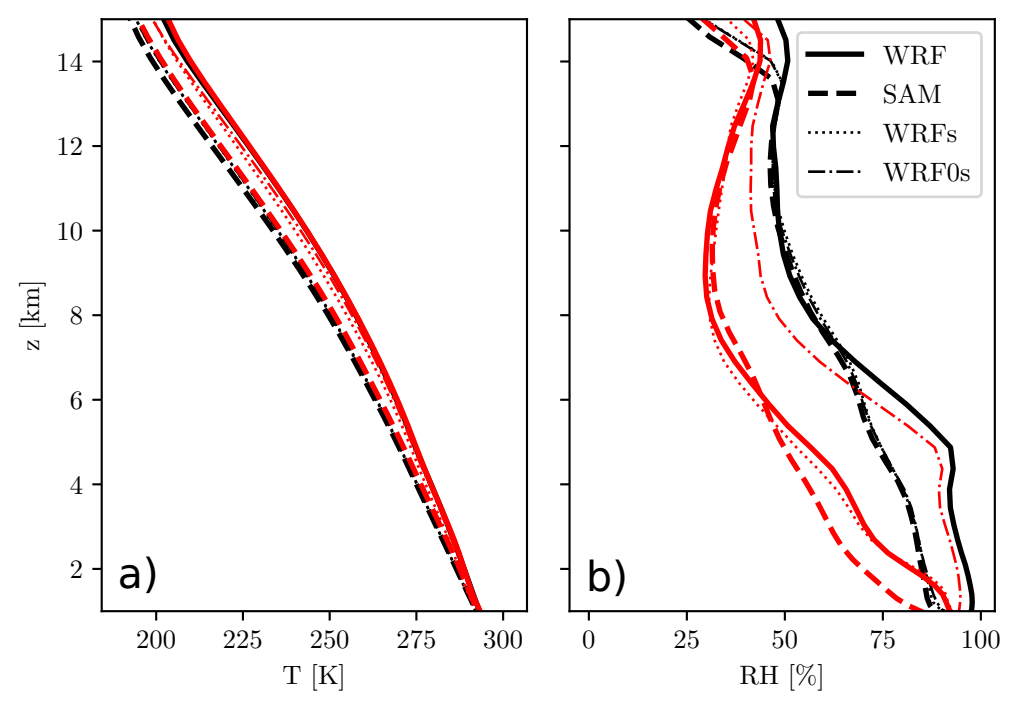
z [km]
14
12
10
8
6
4
2
a)
200
225
250
275
300
T [K]
b)
0
25
50
75
100
RH [%]
WRF
SAM
WRFs
WRF0s

Figure 10.

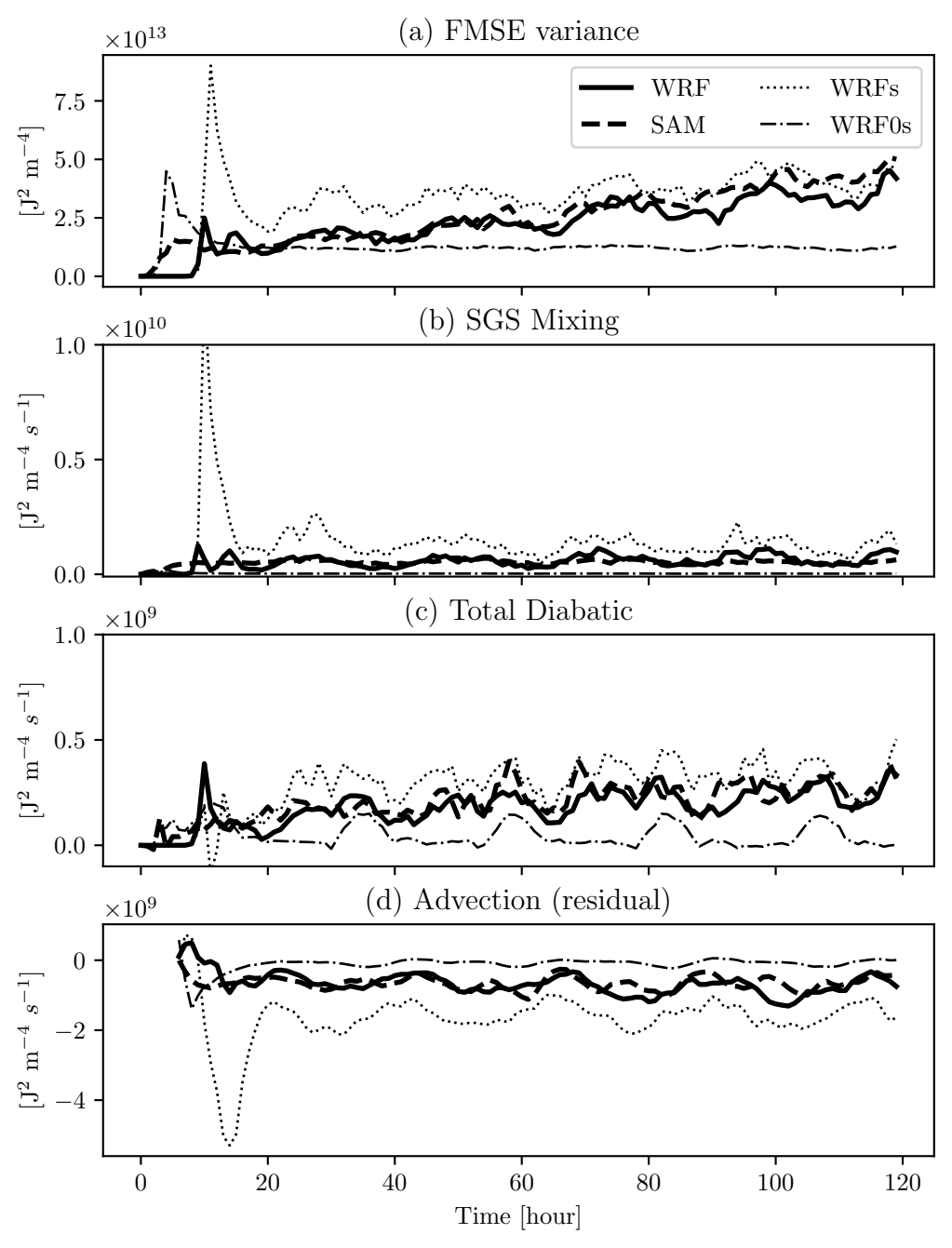
(a) FMSE variance
×10^13
[J^2 m^-4]
7.5
5.0
2.5
0.0
WRF
SAM
WRFs
WRF0s
(b) SGS Mixing
×10^10
[J^2 m^-4 s^-1]
1.0
0.5
0.0
(c) Total Diabatic
×10^9
[J^2 m^-4 s^-1]
1.0
0.5
0.0
(d) Advection (residual)
×10^9
[J^2 m^-4 s^-1]
0
−2
−4
0
20
40
60
80
100
120
Time [hour]

Figure 11.

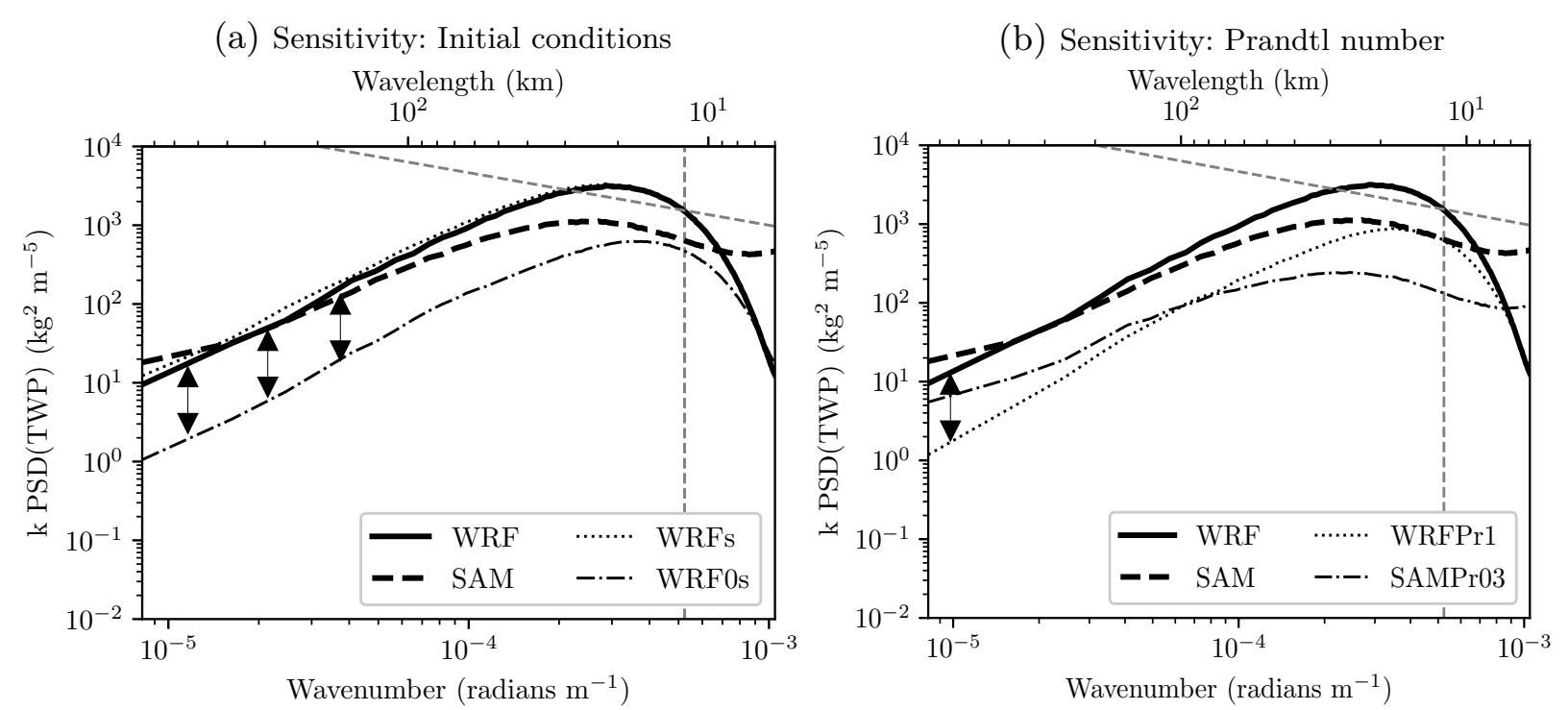
(a) Sensitivity: Initial conditions
Wavelength (km)
10^2
10^1
10^4
10^3
10^2
10^1
10^0
10^{-1}
10^{-2}
k PSD(TWP) (kg^2 m^{-5})
WRF
SAM
WRFs
WRF0s
10^{-5}
10^{-4}
10^{-3}
Wavenumber (radians m^{-1})
(b) Sensitivity: Prandtl number
Wavelength (km)
10^2
10^1
10^4
10^3
10^2
10^1
10^0
10^{-1}
10^{-2}
k PSD(TWP) (kg^2 m^{-5})
WRF
SAM
WRFPr1
SAMPr03
10^{-5}
10^{-4}
10^{-3}
Wavenumber (radians m^{-1})

Figure 12.

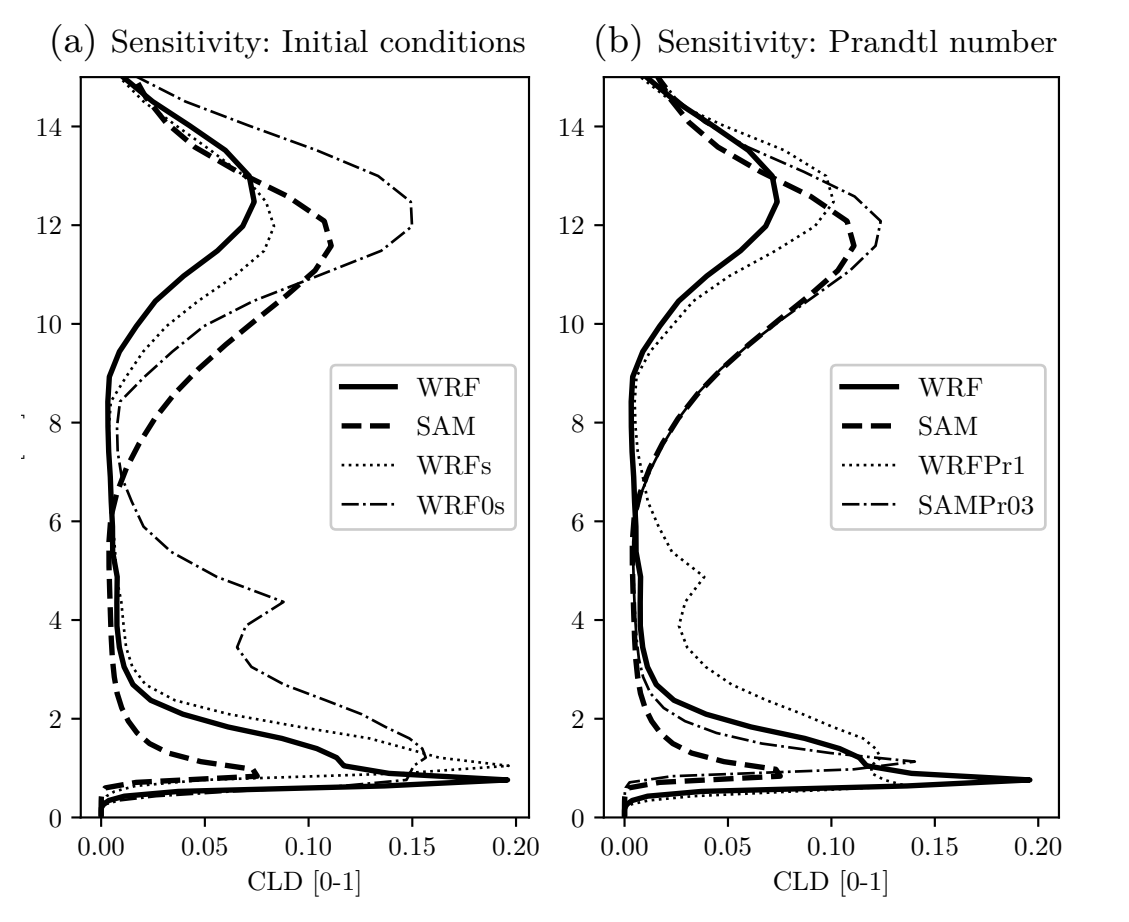
(a) Sensitivity: Initial conditions
(b) Sensitivity: Prandtl number
WRF
SAM
WRFs
WRF0s
WRFPr1
SAMPr03
0
2
4
6
8
10
12
14
0.00
0.05
0.10
0.15
0.20
CLD [0-1]

Figure 13.

(a) WRFPr1

(b) SAMPr03

Y [km]

0

200

400

600

X [km]

X [km]

OLR [W m^{-2}]

80

120

160

200

240

280

Figure 14.

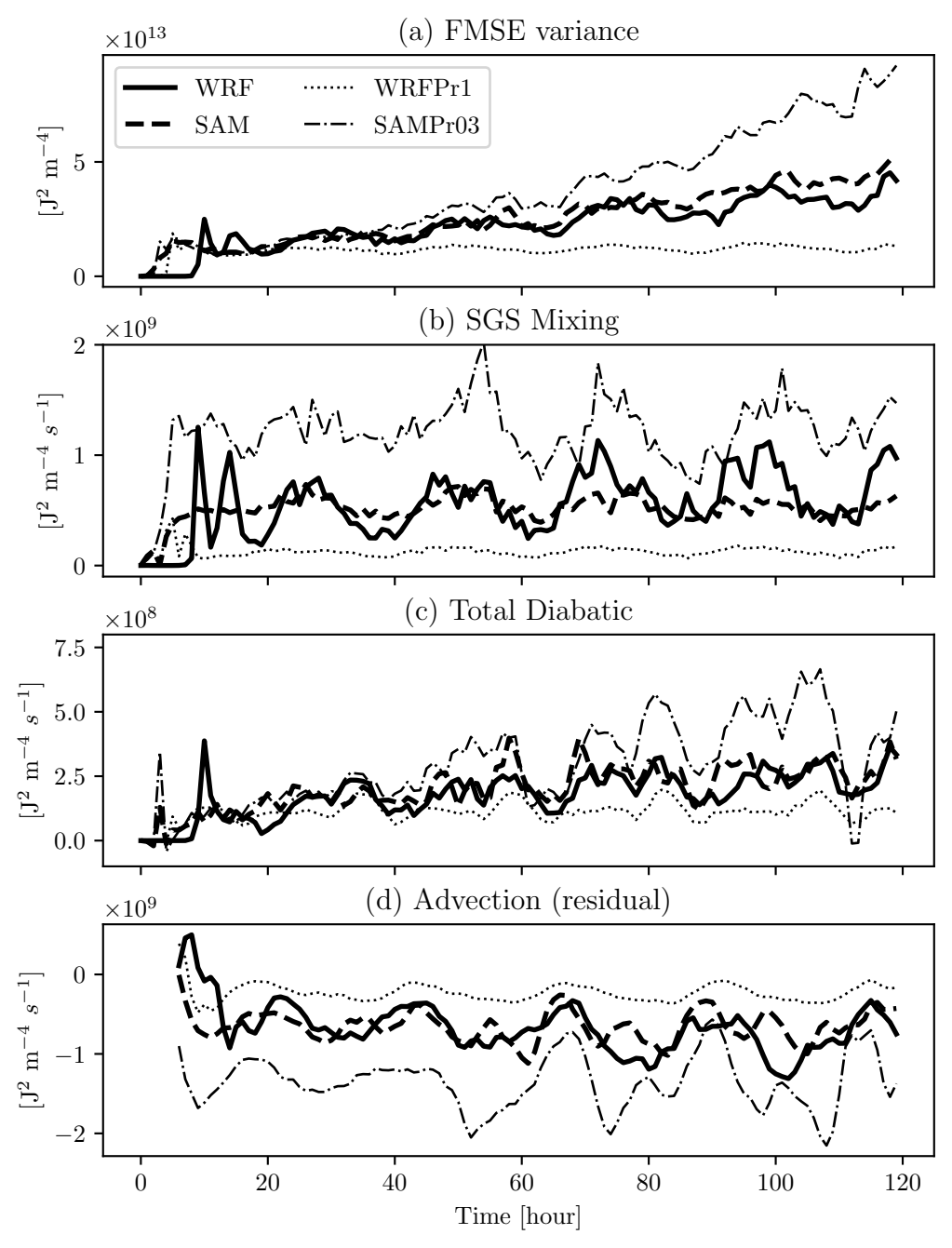
(a) FMSE variance
×10^13
WRF
SAM
WRFPr1
SAMPr03
[J^2 m^-4]
0
5
(b) SGS Mixing
×10^9
[J^2 m^-4 s^-1]
0
1
2
(c) Total Diabatic
×10^8
[J^2 m^-4 s^-1]
0.0
2.5
5.0
7.5
(d) Advection (residual)
×10^9
[J^2 m^-4 s^-1]
−2
−1
0
0
20
40
60
80
100
120
Time [hour]

Figure 15.

(a) WRFh

(b) SAMh

(c) WRF3h

(d) SAM3h

Y [km]

0

200

400

600

X [km]

OLR [W m^{-2}]

80

120

160

200

240

280

Figure 16.

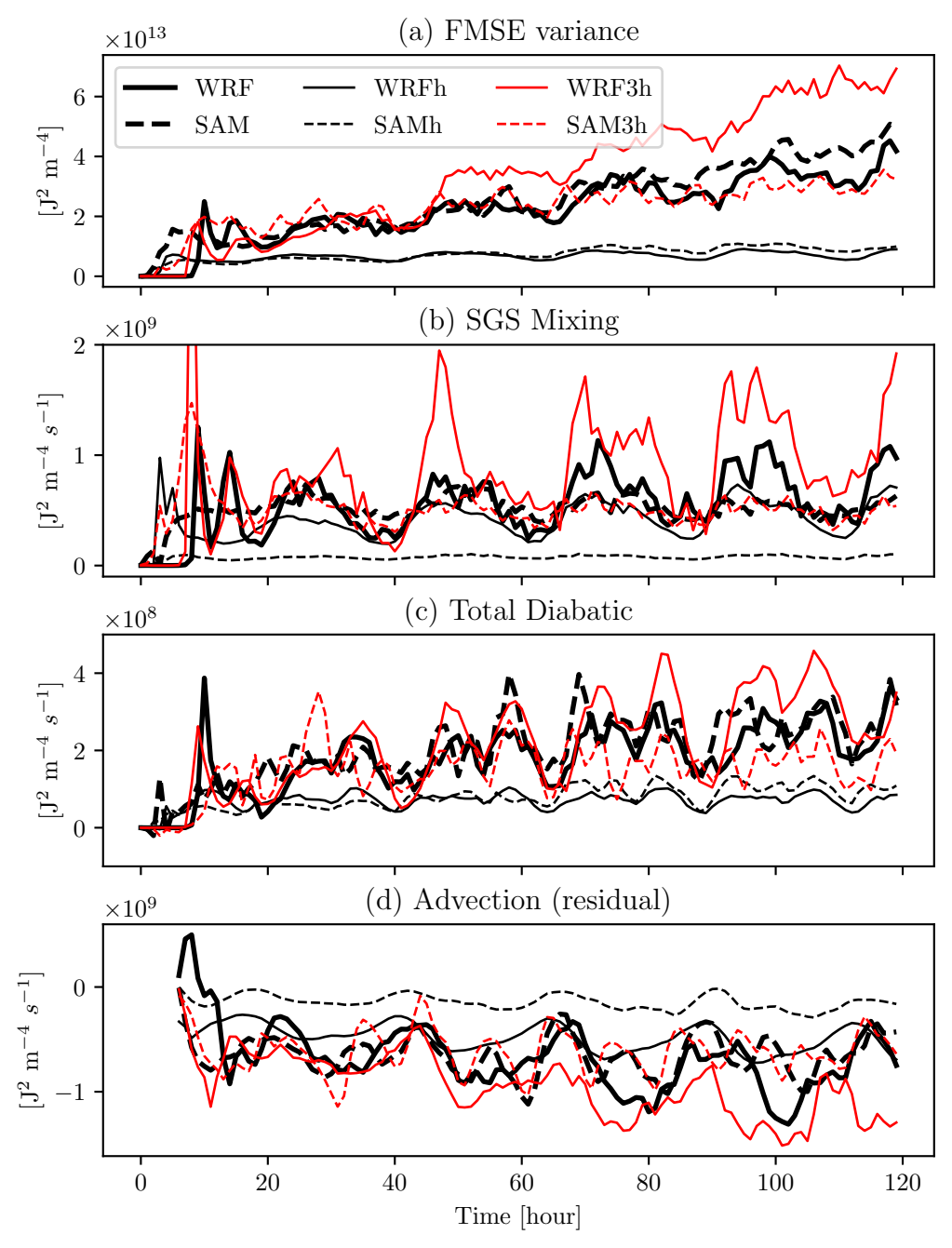
(a) FMSE variance
×10^13
[J^2 m^-4]
WRF
SAM
WRFh
SAMh
WRF3h
SAM3h
(b) SGS Mixing
×10^9
[J^2 m^-4 s^-1]
(c) Total Diabatic
×10^8
[J^2 m^-4 s^-1]
(d) Advection (residual)
×10^9
[J^2 m^-4 s^-1]
Time [hour]

Figure 17.

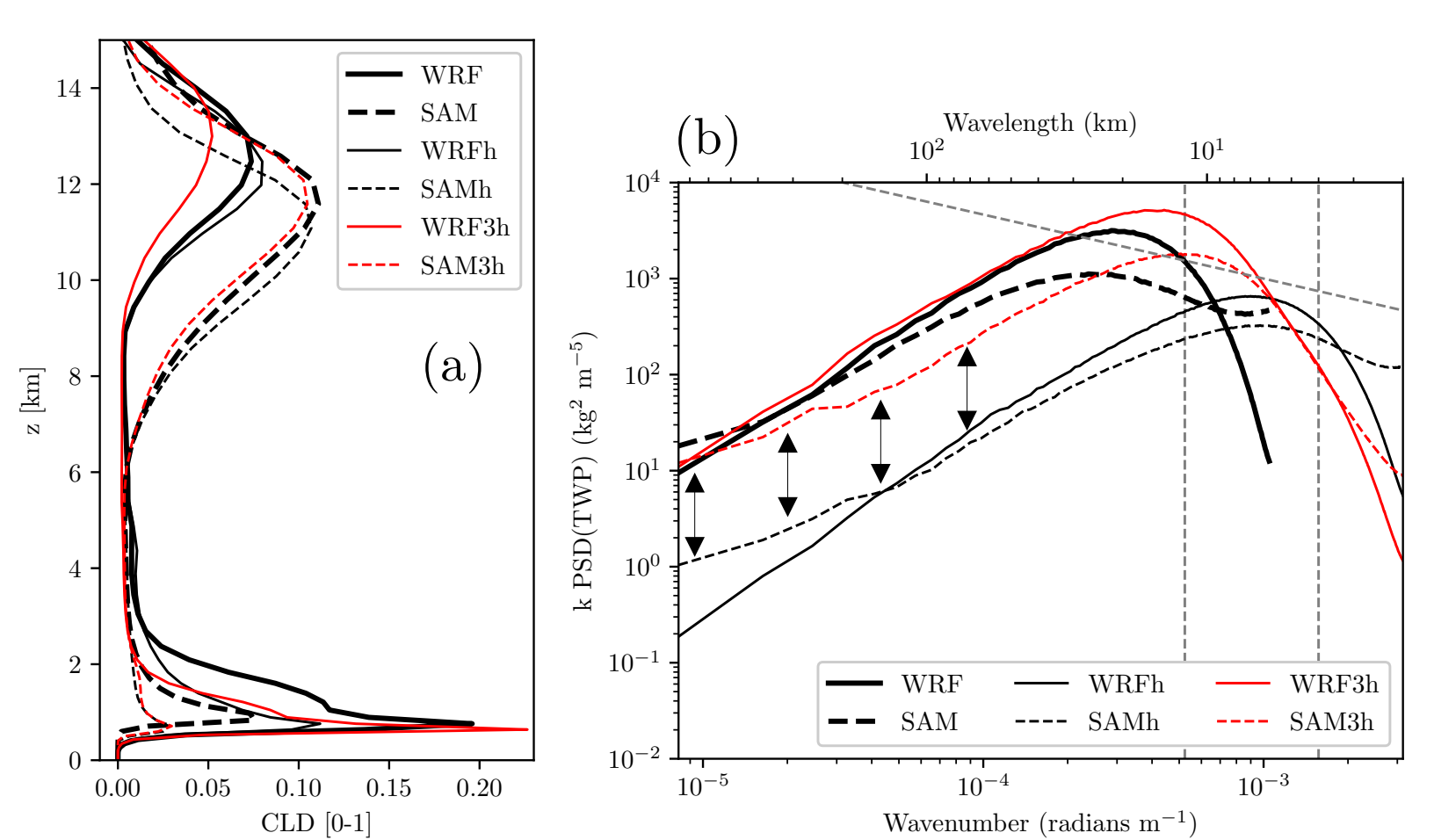
(a)
WRF
SAM
WRFh
SAMh
WRF3h
SAM3h
z [km]
CLD [0-1]
0
2
4
6
8
10
12
14
0.00
0.05
0.10
0.15
0.20
(b)
Wavelength (km)
10^2
10^1
k PSD(TWP) (kg^2 m^{-5})
10^4
10^3
10^2
10^1
10^0
10^{-1}
10^{-2}
10^{-5}
10^{-4}
10^{-3}
Wavenumber (radians m^{-1})
WRF
SAM
WRFh
SAMh
WRF3h
SAM3h